Design of a high sensitivity emitter-detector avalanche photodiode imager using very high transmittance, back-illuminated, silicon-on-sapphire

Alvin G. Stern

Design of a high sensitivity emitter-detector avalanche photodiode imager using very high transmittance, back-illuminated, silicon-on-sapphire

Alvin G. Stern
AG STERN, LLC
Newton, Massachusetts 02467
E-mail: ag_stern@hotmail.com

Abstract. We present a detailed design study for a novel solid-state focal plane array of silicon avalanche photodiodes (APDs) using an advanced silicon-on-sapphire substrate incorporating an antireflective bilayer consisting of crystalline aluminum nitride (AlN) and amorphous, non-stoichiometric, silicon rich, silicon nitride (a-SiN$_{X<1.33}$) between the silicon and sapphire. The substrate supports electrical and optical integration of a nearly 100% quantum efficiency, silicon APD capable of operating with wide dynamic range in dual linear or Geiger-mode, with a gallium nitride (GaN) laser diode in each pixel. The APD device and epitaxially grown GaN laser are fabricated within a crystallographically etched silicon mesa. The high resolution 27 μm emitter-detector pixel design enables single photon sensitive, solid-state focal plane arrays (FPAs), with passive and active imaging capability in a single FPA. The square 27 μm emitter-detector pixel achieves SNR > 10 in active detection mode for Lambert surfaces at 20,000 m. © *2012 Society of Photo-Optical Instrumentation Engineers (SPIE).* [DOI: 10.1117/1.OE.51.6.063206]

Subject terms: silicon APD arrays; back-illuminated; GaN laser diode; silicon-on-sapphire; crystallographically selective etching; monolithic sapphire microlens arrays; emitter-detector pixel; zero optical crosstalk.

Paper 120352 received Mar. 8, 2012; revised manuscript received Apr. 12, 2012; accepted for publication Apr. 18, 2012; published online Jun. 13, 2012.

1 Introduction

There is a growing need in science, industry and medical research for compact, large scale detector arrays capable of imaging with high sensitivity in a passive and active detection mode with detectors providing their own source of short pulse, laser illumination to the area in the scene that is conjugated (using a camera lens for example) back to the respective pixel, providing the laser light pulse. In this design study paper, we demonstrate through detailed calculation means that a novel, back-illuminated photonic device design that optically and electrically integrates a nearly 100% quantum efficiency silicon avalanche photodiode (APD), with a vertical-cavity surface-emitting (VCSEL) gallium nitride (GaN) laser diode in a single pixel will enable imaging with high sensitivity [signal-to-noise ratio (SNR) > 10] near room temperature at $-30\,°C$, in an active detection mode for Lambert surfaces at ranges up to 20,000 m.

The novel emitter-detector pixel design supports a compact, square 27 μm side length silicon APD detector for high resolution, large scale arrays, with each detector capable of wide dynamic range operation in dual linear or Geiger-mode for passive and active two-dimensional (2D) and three-dimensional (3D) imaging. The advanced emitter-detector pixel achieves nearly 100% APD detector quantum efficiency at the laser emission wavelength of $\lambda_0 = 370$ nm, enabled by a very high transmittance silicon-on-sapphire substrate incorporating an antireflective bilayer of crystalline aluminum nitride (AlN) and amorphous, non-stoichiometric, silicon rich, silicon nitride (a-SiN$_{X<1.33}$) that provides optimal

refractive index matching between the silicon and C or R-plane sapphire.[1–5] The sapphire substrate is coated with a $\lambda/4$-MgF$_2$ back-side antireflective layer, to improve the optical power transmittance from air into the sapphire. The design of the very high transmittance Si-(AlN/a-SiN$_{0.62}$)-sapphire substrate with $\lambda/4$-MgF$_2$ back-side antireflective layer is optimized here for peak transmittance into Si at the GaN-VCSEL diode wavelength $\lambda_0 = 370$ nm.[6]

The very high transmittance, back-illuminated Si-(AlN/a-SiN$_{0.62}$)-sapphire substrates with $\lambda/4$-MgF$_2$ back-side antireflective layer, support fabrication of uniform, large scale, high resolution and high sensitivity silicon APD-FPAs designed to operate over a wide dynamic range in dual linear and Geiger-mode with electrically and optically integrated GaN laser diodes in each pixel. When (100) silicon is properly etched with tetramethyl ammonium hydroxide (TMAH) solution through a thermally grown oxide mask, square based pyramidal frustum or mesa arrays result with the four mesa sidewalls of the APD formed by (111) silicon planes that intersect the (100) planes at a crystallographic angle, $\phi_c = 54.7°$.[7] A second anisotropic etching step through a different thermally grown or deposited oxide mask, will yield an inverted pyramidal frustum cavity inside the silicon mesa frustum. The GaN-VCSEL diode is grown epitaxially inside the etched silicon pixel cavity. The APD is fabricated in the remaining silicon mesa using conventional silicon processing technology and is specially designed to operate over a wide dynamic range in a dual-mode, operating in a linear mode with or without internal gain for passive imaging in daylight conditions and in single-photon sensitive Geiger-mode for active or passive imaging under low light level conditions.[5,8] A monolithic sapphire microlens beneath

each pixel is optimized to effectively shape and relay the laser beam to an object of interest while its secondary function is to concentrate reflected radiation from an object into the detector active area and away from the silicon mesa sidewalls, thereby compensating the optical dead space between pixels resulting from the mesa isolation etch. A low resistance aluminum (Al) or copper (Cu) metal anode grid fills the space between pixels and also inhibits direct optical crosstalk between adjacent pixels. In addition to shaping the GaN-VCSEL laser beam and focusing reflected radiation from objects in a scene into the APD active area, the monolithic sapphire microlens reduces indirect optical crosstalk and attendant noise in the array due to multiple reflections in the sapphire substrate of light emitted from the APD multiplication region, by reflecting the APD emitted light back into the detector and reducing the probability of transmission into neighboring pixels.[6] The 27 μm emitter-detector pixel for high quantum efficiency and high resolution passive and active imaging arrays is shown in Fig. 1, using very high transmittance Si-(AlN/a-SiN$_{0.62}$)-sapphire substrate with $\lambda/4$-MgF$_2$ back-side antireflective layer that is optimized primarily for the active detection mode. The GaN-VCSEL diode cavity is formed by AlN/GaN and SiO$_2$/HfO$_2$ distributed Bragg reflector (DBR) mirrors, the latter fabricated on a transparent indium tin oxide (ITO) electrical contact layer.

The 27 μm silicon mesa APD emitter-detector pixel with GaN-VCSEL diode is shown in Fig. 2, comprising an imaging focal plane array that illuminates the area in a scene spatially conjugated back to the pixel by the camera lens. The emitter-detector pixel is therefore capable of providing efficient short pulse laser illumination at the pixel level, to the area in a scene, spatially conjugated back to the pixel providing the short pulse laser illumination. In a large 1024 × 1024 array of emitter-detector pixels of the type shown in Fig. 1, it can be expected that non-uniformities in GaN-VCSEL diode current-voltage (I-V) characteristics will exist, resulting in variations in the optical power output of the lasers from different pixels. If all the laser light sources in
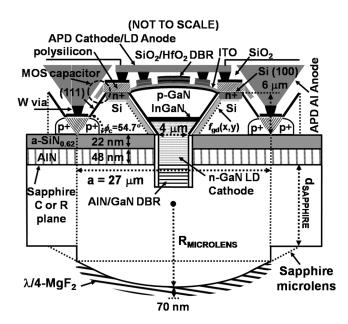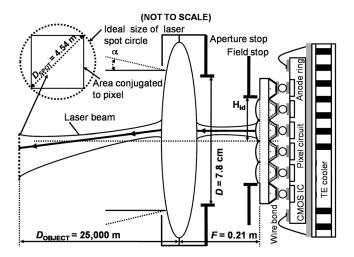

Fig. 2 Operation of FPA comprised of 27 μm emitter-detector pixels illuminating the area in a scene spatially conjugated back to the pixel by the camera lens.

the FPA are made to emit in unison, emulating a flash used to collect 2D intensity images at low light levels by conventional cameras, the resulting non-uniform illumination of areas in a scene can lead to distorted 2D intensity images that might require correction in software. The primary purpose of having a short pulse laser light source in each pixel however, is not for brightening a scene under low light conditions for collecting 2D intensity images, since the APD detectors are already sufficiently sensitive for passive imaging at the lowest natural illumination conditions.[8] The purpose rather of having a short pulse laser light source in each pixel, is for providing an optical pulse to measure the return time-of-flight of the photons reflected from an object in the scene conjugated to the pixel containing the light source, using a range gating technique. The range from the focal plane array to objects in a scene can be measured by delaying arming of the APD in Geiger-mode following an emitted optical pulse from the pixel, by a time interval corresponding to when the optical returns from a specific object distance are expected to arrive, and disarming the APD after a fixed gate-on time interval to set the range gate. A one-bit resolution image is thereby created (digital "1" if an object is present or digital "0" for no object present at the observed distance within the range gate). Active imaging of this type allows constructing a detailed range map for points in the scene based on the collected range data for each point located within the field of view of the imager, in effect creating a 3D image or spatial range map for the field of view. For the method of active 3D imaging described, variations in the optical power output of light sources across the array are less problematic than for collecting a 2D intensity image for example, where information is contained in the relative brightness of the light reflected from objects in the scene, because the 3D image is constructed from statistical data that simply seeks to identify whether an object is present or not at a certain distance in the scene. If light emitters in certain pixels are defective or very dim compared to the other light emitters in the array, then such pixels will not be capable of identifying or registering the presence of objects or areas on an object at equally long ranges with the other normally operating pixels, due to a reduced optical signal being

Fig. 1 High sensitivity 27 μm emitter-detector pixel on very high transmittance, back-illuminated Si-(AlN/a-SiN$_{0.62}$)-Sapphire-(MgF$_2$) substrate.

reflected back on the APD detector, resulting in a loss of spatial resolution and range information.

2 Advanced Silicon-on-Sapphire Substrate Characteristics

The silicon-on-sapphire material system was originally developed for integrated circuit applications however, it also has many ideal attributes for use as a substrate, enabling back-illuminated, solid-state, silicon detector arrays. Sapphire is an anisotropic, dielectric crystal of the negative uniaxial type that is weakly birefringent (n_o-$n_e = 0.008$) and possesses broadband optical transmittance ranging from the deep ultraviolet ($\lambda_0 = 200$ nm) to the midwave IR ($\lambda_0 = 5500$ nm). Sapphire is extremely resilient, supporting thinning below 100 μm, which is an important requirement for high resolution, back-illuminated detector arrays and can be etched using inductively coupled plasma (ICP) to fabricate light focusing microlenses for the emitter-detector devices.[9] Sapphire is chemically resistant to most liquid etchants at room temperature and therefore functions as an ideal etchstop material during liquid anisotropic etching with TMAH solution to define the silicon mesa pixel arrays. To enable high quantum efficiency, back-illuminated silicon detector arrays, the refractive index mismatch between air, sapphire and silicon has to be corrected however. The wide bandgap semiconductor material aluminum nitride (AlN), is closely lattice matched and refractive index matched to both sapphire and silicon and offers the prospect of enabling fabrication of high transmittance (100) silicon-on-(AlN)-sapphire substrates for back-illuminated silicon imagers.[5,10] The $\lambda/4$-AlN antireflective layer improves the back-illuminated optical transmittance from sapphire into the device silicon. A $\lambda/4$-MgF$_2$ antireflective layer can be deposited on the back surface of the thinned sapphire substrate to improve optical transmittance from the ambient into the sapphire. A further improvement on the Si-(AlN)-sapphire substrate design can be achieved by incorporating an antireflective bilayer between sapphire and silicon, consisting of single crystal AlN and amorphous silicon nitride (a-SiN$_X$) having a composition of $x \leq 1.33$. An engineered, non-stoichiometric, silicon rich, amorphous silicon nitride (a-SiN$_X$) layer with N:Si ratio $x = 0.62$, provides nearly optimal refractive index matching in conjunction with the single crystal AlN layer, between sapphire and silicon. The absorption of the a-SiN$_{0.62}$ antireflective layer for thicknesses below 50 nm can be considered negligible for UV wavelengths of $\lambda_0 = 250$ nm and the layer can therefore be modeled in calculations as a lossless dielectric.[6,11] Equation (1) expresses the impedance of a material as a function of the real refractive index $n(\lambda)$ and the absorption coefficient $\alpha(\lambda)$.

$$\eta(\lambda) = \sqrt{\frac{\mu_0}{\varepsilon_0 \left(n(\lambda) - j\frac{1}{2}\frac{\alpha(\lambda)}{k_0} \right)^2}}. \tag{1}$$

To calculate the optical power transmittance of TE and TM waves into silicon for the back-illuminated (MgF$_2$)-sapphire-(AlN/a-SiN$_{0.62}$)-Si substrate optimized for emitter-detector pixel arrays, the full wave transfer matrix M_{STACK} for the material layers in the substrate has to be obtained. This result needs to be put into a scattering matrix form that yields the reflection coefficients for the incident

waves which in turn allow the reflected and transmitted optical power to be calculated.[12] The matrix M_{STACK} for air-(MgF$_2$)-sapphire-(AlN/a-SiN$_{0.62}$)-Si results from multiplying together nine wave transfer matrices including four for propagation through MgF$_2$, sapphire, AlN, SiN$_X$ and five matrices for the material interfaces as shown in Eq. (2).

$$M_{\eta-STACK} = \begin{bmatrix} A & B \\ C & D \end{bmatrix} = M_9 M_8 M_7 M_6 M_5 M_4 M_3 M_2 M_1. \tag{2}$$

The matrices M_1, M_3, M_5, M_7 and M_9 represent wave transfer matrices at the air-MgF$_2$, MgF$_2$-sapphire, sapphire-AlN, AlN-a-SiN$_{0.62}$ and a-SiN$_{0.62}$-silicon interfaces while matrices M_2, M_4, M_6, and M_8 are propagation matrices through MgF$_2$, sapphire, AlN and a-SiN$_{0.62}$ layers having thicknesses optimized to yield maximum transmittance into the device silicon at the GaN-VCSEL diode wavelength $\lambda_0 = 370$ nm. All nine matrices are expressed in terms of the complex impedances of the materials given by Eq. (1). Using a Monte Carlo integration approach, it is possible to calculate the back-illumintated optical transmittance into the APD device silicon as a function of the wavelength, for TE waves normally incident to the sapphire substrate plane of the mesa APD pixel from Fig. 1, as shown in Fig. 3.

The calculation in Fig. 3 shows that the AlN and silicon rich a-SiN$_{0.62}$ antireflective bilayer provides refractive index matching to enable high back-illuminated transmittance into silicon. The AlN/a-SiN$_{0.62}$ antireflective bilayer of 48/22 nm thickness, respectively between sapphire and silicon and 70 nm thick MgF$_2$ antireflective layer between air and sapphire, has been tuned for maximum transmittance at the GaN-VCSEL diode wavelength $\lambda_0 = 370$ nm.

Fabrication of the Si-(AlN/a-SiN$_{0.62}$)-sapphire-(MgF$_2$) wafer substrates represents an ongoing development effort and entails the epitaxial growth using molecular beam epitaxy (MBE) or metal organic chemical vapor deposition (MOCVD) of crystalline AlN either on C-plane or R-plane sapphire with a resulting orientation of C-plane or A-plane AlN, respectively. The amorphous, non-stoichiometric,
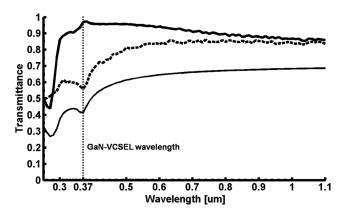

Fig. 3 Optical power transmittance into silicon of a TE wave normally incident from air to the back-illuminated substrate. Air-Si reference plot (thin solid line), Air-MgF$_2$(82 nm)-Sapphire-AlN(82 nm)-Si (dashed line), Air-MgF$_2$(70 nm)-Sapphire-AlN/a-SiN$_{0.62}$(48/22 nm)-Si (thick solid line) are shown.

silicon rich silicon nitride (a-SiN$_{0.62}$) is deposited using low pressure chemical vapor deposition (LPCVD) on the silicon wafer, followed by wafer bonding of the AlN face of the sapphire to the a-SiN$_{0.62}$ face of the silicon wafer. Alternatively, the a-SiN$_{0.62}$ can be deposited via LPCVD directly on top of the crystalline AlN layer grown by MBE or MOCVD on sapphire followed by wafer bonding of the a-SiN$_{0.62}$ face of the (AlN/a-SiN$_{0.62}$)-sapphire to the silicon wafer. The sapphire substrate is subsequently thinned by lapping and polishing using a high precision, linear lapping and polishing machine developed for the task. The $\lambda/4$-MgF$_2$ antireflective layer is deposited on the back surface of the sapphire. The silicon wafer is then lapped and polished to a proper device thickness ranging from 5 to 100 μm.

3 Method of Si-APD/GaN-VCSEL Electrical and Optical Integration

The emitter-detector pixel shown in Fig. 1, consists of a wide dynamic range 27 μm mesa APD with GaN-VCSEL diode epitaxially grown in the crystallographically etched central cavity of the silicon mesa. The APDs share a common, front-side anode contact and laser diodes share a common, front-side cathode contact across an array. In each emitter-detector pixel the silicon APD detector cathode terminal is electrically connected with the GaN-VCSEL diode anode terminal using a metallization layer that in turn becomes connected to the pixel control circuit of a CMOS readout IC using flip-chip bump-bonding. The electrical connection in an emitter-detector pixel between the APD cathode and GaN-VCSEL anode is enabled by the close matching between the forward turn-on voltage of the GaN-VCSEL diode (4 to 5 V) and the reverse silicon APD bias voltage (overbias) above the reverse avalanche breakdown voltage (4 to 5 V) in Geiger-mode. The electrical connection topology allows pixels in the array to be controlled independently or in unison by the electronic readout circuit in the focal plane, as required by the imaging application. The emitter-detector pixels are operated in an active mode by forward biasing the GaN-VCSEL laser diodes while the APDs are turned off. When optical returns from the scene must be detected, the APDs are turned on while the laser diodes are turned off. Operating the emitter-detector pixel by alternately turning on and off the GaN laser and APD detector, requires the common cathode terminal of the laser diodes and common anode terminal of the APDs to be independently accessible to the electronic control circuitry of the focal plane array.

The Si-(AlN/a-SiN$_{0.62}$)-sapphire material system supports electrical isolation between laser diode cathodes and APD anodes. Figure 4 shows how AlN and a-SiN$_{0.62}$ can be used to provide a non-conducting antireflective bilayer for the silicon APDs while n-type GaN, epitaxially grown to the same height as the 48 nm thick AlN layer or 70 nm thick antireflective bilayer, is used to fabricate the common cathode terminal for the laser diodes in the array.

To fabricate the emitter-detector array most directly, a crystalline 48 nm thick AlN layer is epitaxially grown by MBE or MOCVD on a C or R-plane sapphire substrate, followed by the deposition of a 22 nm thick a-SiN$_{0.62}$ layer on the (100) silicon wafer by LPCVD. Before wafer bonding the AlN face of sapphire to the a-SiN$_{0.62}$ face of the silicon wafer, the sapphire substrate is etched anisotropically
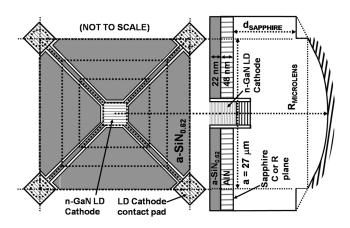

Fig. 4 The n-GaN laser diode cathode is epitaxially grown on the front-side DBR and sapphire substrate.

from the AlN side, using chlorine inductively coupled plasma (ICP) through patterned photoresist, to provide square depressions with 4 μm side length and a depth of 1.58 μm in the sapphire.[9] The photoresist is then removed and silicon dioxide (SiO$_2$) which is selective against AlN and GaN growth on its surface, is blanket deposited by low temperature CVD on the AlN face of the sapphire wafer and etched from the bottom of the square depressions. Selective epitaxial growth of the front-side DBR mirror for the laser resonator cavity on the exposed sapphire substrate, only within the 4 × 4 μm square depressions, can be performed using MBE or MOCVD.[13–15] The MBE method allows epitaxial deposition with the precision of almost single atomic layers only on the exposed sapphire at the base of the square depressions, with the deposited SiO$_2$ blocking growth over the remainder of the wafer substrate.[16] The front-side DBR mirror consists of non-conducting, alternating $\lambda/4$-AlN/GaN layers and has been described.[17] After growing the front-side DBR mirror, photoresist is patterned for the dry etch removal of four diagonal sections and corner squares of the AlN antireflective layer to grow the n-type GaN that will form the cathode of the VCSEL diode. The top most 48 nm thick GaN layer of the DBR is doped n-type and serves as the cathode terminal of the VCSEL diode. It has four branching arms as seen in Fig. 4, that extend to larger pads located at the four corners of the pixel, supporting a shared cathode terminal for all laser diodes in the array, where metal vias shown as dashed circles, contact the laser diode GaN cathode pads at the pixel corners. The a-SiN$_{0.62}$ face of the silicon wafer can now be bonded to the AlN face of the sapphire wafer containing the fabricated front-side DBR and n-type GaN common cathode for the GaN-VCSEL diodes in the array. The silicon is thinned by lapping and polishing to a proper 6 μm device thickness indicated in Fig. 1, followed by anisotropic etching with TMAH to create the silicon mesa pixels with an inverted central cavity. The silicon mesa with etched inverted cavity can be thermally oxidized to passivate the silicon mesa sidewalls, with the SiO$_2$ layer also ensuring that the GaN-VCSEL structure will be grown selectively inside the cavity of the pixel directly above the n-GaN cathode and front-side AlN/GaN DBR mirror. The sloped sidewalls of the silicon mesa cavity are expected to enhance the GaN-VCSEL performance by supporting lateral epitaxial overgrowth (LEO) to uniformly fill the inverted silicon mesa cavity, resulting in
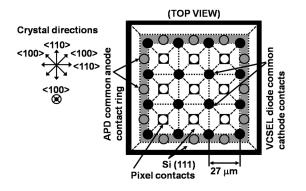
Fig. 5 Example 3×3 pixel emitter-detector chip showing the placement of In bumps for electrical connectivity.

higher quality GaN/InGaN material from the LEO growth.[18] After the GaN-VCSEL device is grown in the silicon mesa cavity, the APD can subsequently be fabricated in the silicon mesa to complete the emitter-detector pixel. Figure 5 shows a top view of the emitter-detector chip, indicating the placement of indium bumps that define the electrical connectivity scheme for the array.[19]

Variations on the above described fabrication approach can exist, for example where the a-SiN$_{0.62}$ layer is deposited on the AlN by LPCVD to form the antireflective bilayer on sapphire before fabricating the front-side DBR mirror and n-GaN cathode. The silicon wafer is subsequently bonded to the a-SiN$_{0.62}$ face of the (AlN/a-SiN$_{0.62}$)-sapphire wafer.

3.1 Gallium Nitride Vertical Cavity Surface Emitting Laser Diode Design and Operating Characteristics

Development of GaN-VCSEL diodes is an active topic of research and only relatively recently, has successful operation of such devices been demonstrated using optical and electrical carrier injection.[20–25] Using optical pumping, Zhou et al. demonstrated room temperature UV lasing at $\lambda_0 = 383$ nm in a GaN-VCSEL structure having an active region with 20 In$_{0.03}$Ga$_{0.97}$N/GaN multiple quantum wells (MQW), showing that it is indeed possible for GaN-VCSELs to emit coherently at such short wavelengths.[21] By increasing the In mole fraction relative to Ga and using an active region with 10 In$_{0.2}$Ga$_{0.8}$N/GaN multiple quantum wells, Lu et al. demonstrated lasing at the blue visible wavelength $\lambda_0 = 462.8$ nm for a current injection GaN-VCSEL diode at 77 Kelvin.[23] The first room temperature, electrical injection GaN-VCSEL diodes were developed by Higuchi et al. in 2008 and Omae et al. in 2009 at the Nichia company and demonstrated continuous CW lasing at $\lambda_0 = 414.4$ nm and $\lambda_0 = 420$ nm, respectively using 2 InGaN/GaN multiple quantum wells.[24,25] The GaN-VCSEL device grown on C-plane sapphire by Higuchi et al. achieved a continuous-wave (CW) optical output power of 0.14 mW and operated for 2 minutes. The GaN-VCSEL device grown on native GaN substrate by Omae et al. resulted in a lower material dislocation density, achieved a continuous CW optical output power of 0.62 mW and operated for 10 minutes. In all of the existing GaN-VCSEL design implementations from Zhou et al., Lu et al., Higuchi et al., and Omae et al., p-GaN and n-GaN material was used directly for carrier

confinement around the InGaN quantum wells rather than the higher bandgap AlGaN material because it is difficult to achieve a low resistivity p-GaN layer, and p-AlGaN is even more resistive.[24] Although higher bandgap AlGaN material can better confine carriers to the quantum wells to enhance the radiative recombination efficiency, its higher resistivity can be problematic in a GaN-VCSEL diode which has a smaller cross-sectional area generally, than an edge-emitting laser diode (LD) device where it is common to use AlGaN as an electron barrier or cladding layer.[26,27]

The AlN/AlGaN/GaN/InGaN material system is ideal for fabricating lasers emitting UVA radiation spanning a wavelength range from 320 nm to 400 nm and the silicon APD is ideal for detecting such radiation. The wavelength range from 350 nm $< \lambda_0 < 400$ nm propagates especially well through water and the atmosphere because light at these wavelengths is not absorbed readily by most atmospheric gases including Ozone (O$_3$).

The current state of the art electrical injection GaN-VCSEL diodes described above are not yet mature technology and are therefore relatively limited in their maximum optical output power as well as in longevity of operation. The main purpose of this design study paper is to show how an advanced optical and electrical integration scheme, enabled by a novel, very high transmittance, back-illuminated silicon-on-sapphire substrate can be used to integrate a relatively simple, GaN-VCSEL structure with InGaN single quantum well (SQW), similar but not identical to the successful GaN-VCSEL structure of Higuchi et al.,[24] with a silicon APD in a novel emitter-detector pixel and to calculate the expected range sensitivity performance of the pixel in an active imaging mode using the built in laser light source. The emitter-detector pixel architecture can readily support more advanced and elaborate GaN-VCSEL diode designs with likely greater output powers than what we present here, using for example not just one but multiple quantum wells in optimized configurations, however, our purpose is not to design the best possible GaN-VCSEL diode. The purpose rather is to show that with a GaN-VCSEL design similar although not identical to what has been already successfully implemented by Japanese researchers, it should already become possible to attain a high sensitivity in detection of objects in the active imaging mode using the laser light source in the pixel.

The GaN-VCSEL diode design presented here is enabled by the silicon-(AlN/a-SiN$_{0.62}$)-sapphire-(MgF$_2$) substrate using crystallographically etched silicon mesa APD pixels with inverted pyramidal cavities for laser diodes as shown in Fig. 6. The GaN-VCSEL diode is designed to emit light directly through the sapphire substrate using the microlens beneath the emitter-detector pixel to shape and relay the laser beam to the camera lens.

The laser diode emission wavelength is selected for $\lambda_0 = 370$ nm since this wavelength combines the ideal attributes of being invisible to the human eye, propagating well through ordinary glass, the earth's atmosphere and also through water.[28,29] The GaN-VCSEL diode design in Fig. 6 is based on a single quantum well (SQW) of In$_{0.02}$Ga$_{0.98}$N having thickness $L_z = 10$ nm, and located at an antinode of the 8λ resonator cavity between the upper p-GaN anode and lower n-GaN cathode. The composition of the InGaN quantum well supports a lasing wavelength of $\lambda_0 = 370$ nm.
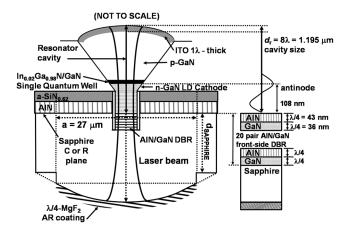
Fig. 6 The GaN laser diode in each emitter-detector pixel has a single quantum well (SQW) of $In_{0.02}Ga_{0.98}N$ supporting a lasing wavelength of $\lambda_0 = 370$ nm. The resonator cavity is formed using a 20-pair epitaxially grown, front-side, partially reflective DBR mirror allowing light to be emitted through the sapphire substrate and collimated by the microlens.

The In to Ga ratio can be determined from the bowing Eq. (3) with constants given in Table 1.[30]

$$E_{g(In_xGa_{(1-x)}N)} = (x)E_{g(In)} + (1-x)E_{g(GaN)} - Bx(1-x). \quad (3)$$

Uncertainty still exists regarding the true value of the InN bandgap, although it is believed to be close to 0.7 eV. The bowing parameter B, in Eq. (3) depends on the epitaxial crystal growth method as well as on the strain in the InGaN material.

The design of the distributed Bragg reflector (DBR) mirrors forming the spherical-planar cavity of the GaN-VCSEL diode has been described previously, where the front-side AlN/GaN DBR has reflectance $R_1 = 99.79\%$ and the backside SiO_2/HfO_2 DBR has reflectance $R_2 = 99.99\%$.[17] The curvature of the spherical sapphire microlens is designed and optimized for shaping and relaying the pixel laser beam to the camera lens as well as for focusing optical returns into the detector silicon. A nearly optimal design of the spherical microlens is shown in Fig. 7. Although the microlens is spherical, the radius offset parameter e, can be adjusted as needed to shape the beam. By enlarging e, the radius R_{ML} of the spherical microlens is reduced, however, the "bulge" in the microlens extending beyond the planar sapphire substrate having thickness $d_{SAPPHIRE} = 50$ μm, increases. The net effect of increasing e, is to increase the curvature of the microlens. As a practical matter, it is not trivial to fabricate a microlens requiring such precise geometry, and especially full arrays for 1–16 Megapixels. Sapphire

Table 1 Bowing equation parameter values at room temperature.

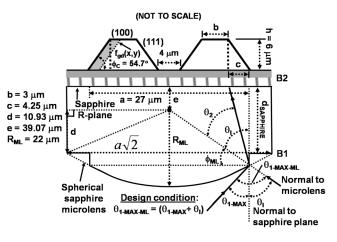| Parameter	Value
In composition parameter: x	0.02
Bowing parameter: B	1.01 eV
Indium bandgap: $E_{g(In)}$	0.77 eV
Gallium nitride bandgap: $E_{g(GaN)}$	3.43 eV

Fig. 7 Geometry of the sapphire microlens intended for collimating the laser beam and focusing optical returns.

microlenses that provide diffraction limited performance have been fabricated however, using lithographically patterned photoresist and ICP etching.[9] Such methods could be adapted for fabricating the lenses in Fig. 7.

The laser beam that exits from the spherical-planar resonator cavity through the AlN/GaN DBR, has to be shaped and relayed first by the microlens and subsequently by the camera lens toward the area on the scene conjugated back to the pixel as shown in Fig. 2. The curvature of the sapphire microlens is optimized by calculating the Gaussian beam parameters consisting of the beam radius and width, using the ABCD law given in Eq. (4).[12]

$$q_2 = \frac{Aq_1 + B}{Cq_1 + D}. \quad (4)$$

In Eq. (4), the letters A, B, C and D represent the elements from matrix M that describes an arbitrary paraxial system. The parameter q_1 in Eq. (4) describes the beam radius and width incident to the optical system, while parameter q_2 describes the beam after transmission through the system. The parameter q is given by Eq. (5).

$$q(z) = \left[\frac{1}{R(z)} - j\frac{\lambda}{\pi W^2(z)}\right]^{-1}. \quad (5)$$

Using Eq. (4) together with Eq. (5), it is possible to calculate the TEM_{00} Gaussian beam parameters from the laser cavity to the illuminated scene. Figure 8 illustrates important locations along the beam path through the paraxial system. The numbered q-parameters in Fig. 8 provide the values of the beam radius and waist at the different locations along the path of propagation. Parameters q_1 and q_2 describe the beam at the back and front-side boundaries, respectively of the resonator cavity. Parameter q_3 describes the beam at the exit plane of the DBR while q_4 and q_5 describe the beam before and after the concave boundary (from beam's perspective), of the microlens with MgF_2 antireflective layer. Parameters q_6 and q_7 describe the beam before and after propagation through the camera lens while q_8 describes the beam at the object distance in the imaged scene. Table 2 provides the calculated beam radii and waist dimensions for the locations indicated in Fig. 8.

The results in Table 2 confirm that the unique emitter-detector pixel architecture proposed here, using the
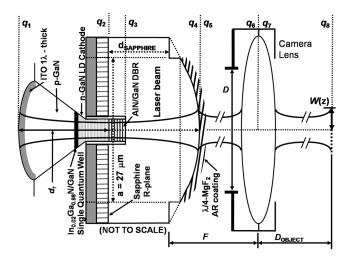
Fig. 8 The radius of curvature and beam waist is known by calculating the q-parameters at the indicated locations.

silicon-on-sapphire material system with novel AlN/a-SiN$_{0.62}$ antireflective bilayer, and epitaxially grown GaN-VCSEL inside of an inverted, crystallographically etched, silicon cavity, will be capable of relaying a laser beam of appropriate size to an object in a scene. The effective laser beam diameter at the object, located at a distance of 25,000 m from the camera is calculated to be 3.18 m. The optimal beam diameter required to fully cover the area in the scene conjugated back to the pixel would be 4.54 m as shown in Fig. 2. To achieve the results in Table 2, only two design parameters were adjusted, namely, the radius of curvature of the back-side of the resonator cavity and the curvature of the spherical microlens. Assuming the two fabrication challenges of proper back-side resonator curvature and microlens curvature are resolved, it will be possible to relay a laser spot of correct size from each emitter-detector pixel to the area in a scene spatially conjugated back to the pixel. It will be shown in Sec. 3.2 that despite a reduction in the silicon mesa volume of each pixel needed to

Table 2 Laser beam parameters.

*Beam Parameter	TEM$_{00}$ beam radius of curvature	TEM$_{00}$ beam width, $2W(z)$
q_1	$-(3.5 \times d_{CAVITY}) = -4.18 \times 10^{-6}$ m	697.2×10^{-9} m
q_2	∞	589.2×10^{-9} m
q_3	3.79×10^{-6} m	802.2×10^{-9} m
q_4	60.73×10^{-6} m	27.0×10^{-6} m
q_5	-153.4×10^{-6} m	27.0×10^{-6} m
q_6	0.209 m	37.22×10^{-3} m
q_7	-289.87 m	37.22×10^{-3} m
q_8	2.47×10^4 m	3.18 m

*Camera lens focal length $F = 0.21$ m and the distance of the object in the scene $D_{OBJECT} = 25,000$ m.

accommodate the VCSEL diode, the APD detector will be capable of operating with high quantum efficiency and high sensitive-area-fill-factor.

The expected threshold current i_t and optical output power P_o from the GaN-VCSEL diode design shown in Fig. 6 with In$_{0.02}$Ga$_{0.98}$N single quantum well, can be estimated using a straightforward analysis and model for the wurtzite quantum well with parabolic conduction bands and non-parabolic valence bands for growth on a C-plane substrate. The simplified analysis presented here is not meant as a substitute for more rigorous engineering software device simulation of the GaN-VCSEL device with the Synopsis MEDICI tool for example that solves the carrier transport equations from the full energy band model for either polar C-plane or non-polar A-plane InGaN/GaN material. The theory of wurtzite InGaN/GaN quantum well full band models for polar (C-plane), non-polar (A and M-plane) and semi-polar material can be used to perform accurate simulations for GaN-VCSEL diode structures.[31–35] Rigorous design simulation for an optimized GaN-VCSEL diode device is beyond the scope of this paper, that seeks only to verify whether the optical and electrical integration scheme enabled by the high transmittance silicon-(AlN/a-SiN$_{0.62}$)-sapphire-(MgF$_2$) substrate, using the basic single quantum well GaN-VCSEL device structure similar to the first successful room temperature, current injection GaN-VCSEL device reported by Higuchi et al.,[24] can be expected to provide sufficient levels of illumination to objects in a scene to detect them with high sensitivity over long ranges. The theory of InGaN/GaN wurtzite material and quantum wells is discussed, followed by the method used here to simplify the analysis of the single quantum well GaN-VCSEL diode for estimating i_t and P_o.

The theoretical model for wurtzite semiconductors such as InGaN/GaN grown on C-plane sapphire, used for calculating the full band structure of a quantum well within the 6×6 multiband effective mass theory that takes into consideration the biaxial strain is described.[32,33] The effective mass Hamiltonian for the conduction band which is assumed to be parabolic is given in Eq. (6).

$$H_c(\vec{k}_t, k_z) = \frac{\hbar^2}{2}\left(\frac{k_t^2}{m_e^t} + \frac{k_z^2}{m_e^z}\right) + E_c^0 + P_{ce}. \quad (6)$$

In Eq. (6), $\boldsymbol{k}_t = -i\nabla_t$, $k_z = -i\partial/\partial z$ are wavevectors. The quantity $k_t = (k_x^2 + k_y^2)^{0.5}$ is the magnitude of the wavevector in the x-y plane of the quantum well, where z is the [0001] growth direction along the C-axis. The quantity $\hbar$ is the reduced Planck constant, m_e^t and m_e^z are the transverse and longitudinal effective masses for the electron, respectively. The energy of the conduction band-edge without strain denoted E_c^0 and hydrostatic energy shift P_{ce} from Eq. (6), are given in Eqs. (7) and (8), respectively.

$$E_c^0 = E_v^0 + \Delta_1 + \Delta_2 + E_g. \quad (7)$$

$$P_{ce} = a_{cz}\varepsilon_{zz} + a_{ct}(\varepsilon_{xx} + \varepsilon_{yy}). \quad (8)$$

In Eq. (7), E_v^0 is the reference energy of a semiconductor taken as zero, Δ_1 is the crystal field energy, Δ_2 is the spin orbit energy, E_g is the bandgap energy and P_{ce} is the hydrostatic energy shift of the conduction band. In

Eq. (8), a_{cz} and a_{ct} are the deformation potentials in the conduction band, parallel and perpendicular to the C-axis, respectively, and ε_{ij} are strain tensor elements with $\varepsilon_{ij} = 0$ for $i \neq j$. The latter assumption is valid for a strained layer wurtzite crystal grown pseudomorphically in the [0001] direction and also for a wurtzite layer having an external in-plane biaxial stress T. The conduction band-edge with strain E_c, will have a hydrostatic energy shift given in Eq. (9).

$$E_c = E_c^0 + P_{ce}. \tag{9}$$

In Eq. (9), E_c^0 is the conduction band-edge without strain defined in Eq. (7) and P_{ce} is the hydrostatic energy shift of the conduction band defined in Eq. (8). The effective mass, block-diagonalized Hamiltonian matrix derived using the $k \cdot p$ method, for the valence band of a bulk, strained-layer, wurtzite semiconductor is given in Eq. (10) for the bases $|1>, |2>, |3>, |4>, |5>, |6>$.[32]

$$H_v(\vec{k}_t, k_z)$$

$$= \begin{pmatrix} F & K_t & -iH_t & & & \\ K_t & G & \Delta - iH_t & & 0 & \\ iH_t & \Delta + iH_t & \lambda & & & \\ & & & F & K_t & iH_t \\ & 0 & & K_t & G & \Delta + iH_t \\ & & & -iH_t & \Delta - iH_t & \lambda \end{pmatrix}. \tag{10}$$

The 6×6 block-diagonalized Hamiltonian matrix of Eq. (10), is comprised of a 3×3 upper matrix H_v^U and a 3×3 lower matrix H_v^L with $H_v^U = (H_v^L)^* = (H_v^L)'$ and where $*$ means complex conjugate while the apostrophe (') signifies a transpose. The elements of the matrix in Eq. (10) can be defined as shown in Eq. (11).

$$F = \Delta_1 + \Delta_2 + \frac{\hbar^2}{2m_0}(A_1 k_z^2 + A_2 k_t^2) + D_1 \varepsilon_{zz}$$

$$+ D_2(\varepsilon_{xx} + \varepsilon_{yy}) + \frac{\hbar^2}{2m_0}(A_3 k_z^2 + A_4 k_t^2) + D_3 \varepsilon_{zz}$$

$$+ D_4(\varepsilon_{xx} + \varepsilon_{yy})$$

$$G = \Delta_1 - \Delta_2 + \frac{\hbar^2}{2m_0}(A_1 k_z^2 + A_2 k_t^2) + D_1 \varepsilon_{zz}$$

$$+ D_2(\varepsilon_{xx} + \varepsilon_{yy}) + \frac{\hbar^2}{2m_0}(A_3 k_z^2 + A_4 k_t^2) + D_3 \varepsilon_{zz}$$

$$+ D_4(\varepsilon_{xx} + \varepsilon_{yy})$$

$$\lambda = \frac{\hbar^2}{2m_0}(A_1 k_z^2 + A_2 k_t^2) + D_1 \varepsilon_{zz} + D_2(\varepsilon_{xx} + \varepsilon_{yy})$$

$$K_t = \frac{\hbar^2}{2m_0}(A_5 k_t^2) \qquad H_t = \frac{\hbar^2}{2m_0}(A_6 k_z k_t)$$

$$\Delta = \sqrt{2}\Delta_3. \tag{11}$$

In Eq. (11), m_0 is the mass of the electron, $\hbar$ is the reduced Planck constant, $A_1 - A_6$ are the valence effective mass parameters for holes and $D_1 - D_4$ are the deformation potentials for wurtzite semiconductors. The quantity Δ_1 is the crystal field energy, Δ_2 is the spin orbit energy and Δ_3 represents a spin-orbit interaction. The relationship between stress τ and strain ε for a hexagonal crystal such as InGaN/GaN is given in Eq. (12).[36]

$$\begin{bmatrix} \tau_{xx} \\ \tau_{yy} \\ \tau_{zz} \\ \tau_{yz} \\ \tau_{zx} \\ \tau_{xy} \end{bmatrix} = \begin{bmatrix} C_{11} & C_{12} & C_{13} & & & \\ C_{12} & C_{11} & C_{13} & & 0 & \\ C_{13} & C_{13} & C_{33} & & & \\ & & & C_{44} & & \\ & 0 & & & C_{44} & \\ & & & & & \frac{C_{11}-C_{44}}{2} \end{bmatrix} \times \begin{bmatrix} \varepsilon_{xx} \\ \varepsilon_{yy} \\ \varepsilon_{zz} \\ \varepsilon_{yz} \\ \varepsilon_{zx} \\ \varepsilon_{xy} \end{bmatrix}. \tag{12}$$

In Eq. (12), C_{ij} represent the stiffness constants, τ represents the stress tensor and ε represents the strain tensor. For a strained layer, wurtzite crystal grown pseudomorphically in the [0001] direction, ε is a diagonal tensor as can be verified from Eq. (12), where the diagonal elements of ε are given by Eq. (13).

$$\varepsilon_{xx} = \varepsilon_{yy} = \frac{a_s - a_w}{a_w} \qquad \varepsilon_{zz} = -\frac{2C_{13}}{C_{33}}\varepsilon_{xx}. \tag{13}$$

In Eq. (13), a_s and a_w are the lattice constants of the substrate GaN and quantum well material layer $In_{0.02}Ga_{0.98}N$, respectively. The relation for ε_{zz} in Eq. (13) is obtained due to $\tau_{zz} = 0$. For a wurtzite layer under an external biaxial stress $T = \tau_{xx} = \tau_{yy}$, ε is also a diagonal tensor as can be verified from Eq. (12), where diagonal elements of ε are given by Eq. (14).

$$\varepsilon_{xx} = \varepsilon_{yy} = \left(C_{11} + C_{12} - 2\frac{C_{13}^2}{C_{33}}\right)^{-1} T$$

$$\varepsilon_{zz} = -2\frac{C_{13}}{C_{33}}\left(C_{11} + C_{12} - 2\frac{C_{13}^2}{C_{33}}\right)^{-1} T. \tag{14}$$

To calculate the valence band structures for the wurtzite material, it is necessary to know the band structure parameters $A_1 - A_6$, $D_1 - D_4$ and $\Delta_1 - \Delta_3$ that are generally obtained from a first principle theoretical calculation using for example, the self-consistent, full potential, linearized-augmented, plane-wave method within the local density-functional approximation to calculate the band-edge dispersion curves.[31] Using a cubic approximation, allows the number of known band structure parameters to be reduced to just five as shown in Eq. (15).

$$A_1 - A_2 = -A_3 = 2A_4$$

$$A_3 + 4A_5 = \sqrt{2}A_6$$

$$D_1 - D_2 = -D_3 = 2D_4$$

$$\Delta_2 = \Delta_3. \tag{15}$$

From Eq. (15), it is evident that knowing $A_1, A_2, A_5, D_1, D_2,$ Δ_1, Δ_2 is sufficient to calculate the valence band structure.

The upper 3×3 Hamiltonian H_v^U and lower 3×3 Hamiltonian H_v^L from Eq. (10) are measured with respect to the reference energy $E_v^0 = 0$ eV and the valence band-edge energies are given by Eq. (16) taking strain into consideration.

$$E_1^0 = E_v^0 + \Delta_1 + \Delta_2 + D_1\varepsilon_{zz} + D_2(\varepsilon_{xx} + \varepsilon_{yy}) + D_3\varepsilon_{zz}$$
$$+ D_4(\varepsilon_{xx} + \varepsilon_{yy})$$

$$E_2^0 = E_v^0 + \frac{\Delta_1 - \Delta_2 + D_3\varepsilon_{zz} + D_4(\varepsilon_{xx} + \varepsilon_{yy})}{2} + D_1\varepsilon_{zz}$$
$$+ D_2(\varepsilon_{xx} + \varepsilon_{yy})$$
$$+ \sqrt{\left[\frac{\Delta_1 - \Delta_2 + D_3\varepsilon_{zz} + D_4(\varepsilon_{xx} + \varepsilon_{yy})}{2}\right]^2 + 2\Delta_3^2}$$

$$E_3^0 = E_v^0 + \frac{\Delta_1 - \Delta_2 + D_3\varepsilon_{zz} + D_4(\varepsilon_{xx} + \varepsilon_{yy})}{2} + D_1\varepsilon_{zz}$$
$$+ D_2(\varepsilon_{xx} + \varepsilon_{yy})$$
$$- \sqrt{\left[\frac{\Delta_1 - \Delta_2 + D_3\varepsilon_{zz} + D_4(\varepsilon_{xx} + \varepsilon_{yy})}{2}\right]^2 + 2\Delta_3^2}. \tag{16}$$

In Eq. (16), the valence band-edge energies with strain effects present are given as E_1^0, E_2^0 and E_3^0. In Eq. (16), m_0 is the electron mass, $\hbar$ is the reduced Planck constant, Δ_1 is the crystal field energy, Δ_2 is the spin orbit energy, Δ_3 represents a spin-orbit interaction, reference energy $E_v^0 = 0$ eV, $D_1 - D_4$ are the deformation potentials for wurtzite semiconductors and ε_{ij} are strain tensor elements.

For a layer of $In_{0.02}Ga_{0.98}N$ comprising a single quantum well between two thick GaN layers (p-GaN and n-GaN) as shown in Fig. 6, the strain will be compressive due to the lattice constant of $In_{0.02}Ga_{0.98}N$ being greater than that of GaN expressed as $a_w > a_s$ from Eq. (13). The bandgap with strain is therefore determined according to Eq. (17).

$$E_c - E_1^0 = E_g + P_{ce} - [D_3\varepsilon_{zz} + D_4(\varepsilon_{xx} + \varepsilon_{yy}) + D_1\varepsilon_{zz}$$
$$+ D_2(\varepsilon_{xx} + \varepsilon_{yy})]. \tag{17}$$

In Eq. (17), E_c is the conduction band-edge with strain defined in Eq. (9) and E_1^0 is the valence band-edge with strain defined in Eq. (16). The wavefunction of the electron is given according to Eq. (18).

$$\Psi_{n,k_t}^{c\eta}(z) = \frac{e^{ik_t \bullet r_t}}{\sqrt{A}}\phi_n(z)|S,\eta\rangle. \tag{18}$$

In Eq. (18), k_t is the transverse wavevector, r_t is the two-dimensional position vector, A is the area of the quantum well in the x-y plane, ϕ_n is the envelope function of the nth conduction band, $\eta = \uparrow$ or $\downarrow$ is the electron spin and

S is the spherically symmetric Bloch wavefunction of the crystal. The self-consistent band structure and wavefunctions can be obtained by solving the Schroedinger equation with the Poisson equation by iteration. The conduction subband energies $E_n^c = E_n^c(k_t = 0)$ can be obtained however, by solving Eq. (19) which must be satisfied for the envelope function.

$$H_c(k_t = 0, k_z = -i\partial/\partial z)\phi_n(z) = E_n^c\phi_n(z). \tag{19}$$

In Eq. (19), H_c is the effective mass Hamiltonian for the conduction band from Eq. (6), ϕ_n is the envelope function of the nth conduction subband which is normalized according to Eq. (20).

$$\int dz|\phi_n(z)|^2 = 1 \tag{20}$$

Solving Eq. (19) at $k_t = 0$, and independent of the electron spin, yields the rather well known Eq. (21) describing the parabolic conduction band.

$$E_n^c(k_t) \approx E_n^c(k_t = 0) + \frac{\hbar^2 k_t^2}{2m_{e,w}^t}. \tag{21}$$

In Eq. (21), $m_{e,w}^t$ is the electron effective mass in the well region parallel to the quantum well.

The wavefunction of the hole is given in Eq. (22) for the upper Hamiltonian H^U and in Eq. (23) for the lower Hamiltonian H^L.

$$\Psi_m^U(z; k_t) = \frac{e^{ik_t \bullet r_t}}{\sqrt{A}}[g_m^{(1)}(z; k_t)|1\rangle + g_m^{(2)}(z; k_t)|2\rangle$$
$$+ g_m^{(3)}(z; k_t)|3\rangle]. \tag{22}$$

$$\Psi_m^L(z; k_t) = \frac{e^{ik_t \bullet r_t}}{\sqrt{A}}[g_m^{(4)}(z; k_t)|4\rangle + g_m^{(5)}(z; k_t)|5\rangle$$
$$+ g_m^{(6)}(z; k_t)|6\rangle]. \tag{23}$$

In Eqs. (22) and (23), $g_m^{(i)}$, are the envelope functions where m represents the valence subband. The valence subband energies for the upper Hamiltonian $E_m^U(k_t)$ and for the lower Hamiltonian $E_m^L(k_t)$ can be determined by solving Eqs. (24) and (25), respectively.

$$\sum_{j=1}^{3}\left[H_{ij}^U\left(k_z = -i\frac{\partial}{\partial z}\right) + \delta_{ij}E_v^0(z)\right]g_m^{(j)}(z; k_t)$$
$$= E_m^U(k_t)g_m^{(i)}(z; k_t). \tag{24}$$

$$\sum_{j=4}^{6}\left[H_{ij}^L\left(k_z = -i\frac{\partial}{\partial z}\right) + \delta_{ij}E_v^0(z)\right]g_m^{(j)}(z; k_t)$$
$$= E_m^L(k_t)g_m^{(i)}(z; k_t). \tag{25}$$

In Eq. (24), $i = 1, 2, 3$ and in Eq. (25), $i = 4, 5, 6$ where $g_m^{(i)}$ represents envelope functions for the mth valence subbands and E_v^0 represents the potential energy for the valence band offset of the quantum well. In Eq. (24), $E_m^U(k_t)$ represents

the valence subband energies corresponding to the upper Hamiltonian H^U and in Eq. (25), $E_m^L(k_t)$ represents the valence subband energies corresponding to the lower Hamiltonian H^L for the valence band, described by the 6×6 block-diagonalized Hamiltonian matrix given in Eq. (10). The envelope functions $g_m^{(i)}$ for the mth valence subbands are normalized according to Eq. (26).

$$\sum_{i=1}^{3} \int \mathrm{d}z |g_m^{(i)}(z; k_t)|^2 = 1, \quad \sum_{i=4}^{6} \int \mathrm{d}z |g_m^{(i)}(z; k_t)|^2 = 1.$$
$$(26)$$

Solving the effective mass equations for the valence subband structure given in Eqs. (24) and (25) can be accomplished most directly using the finite difference method to yield the non-parabolic valence subbands in the wurtzite material grown on the C-plane.[33] The above theoretical model for wurtzite semiconductors such as InGaN/GaN grown on C-plane sapphire, used for calculating the full band structure of a quantum well within the 6×6 multiband effective mass theory that takes into consideration the biaxial strain, can also be used to take into consideration other effects in the material. Refinements of the model include in addition to the biaxial strain, considering the spontaneous (SP) and strain induced piezoelectric (PZ) polarization fields along the [0001] or C-axis direction which can be on the order of megavolts/cm. The internal electrical fields due to SP and PZ can be included in Eq. (19) for the conduction band and in Eqs. (24) and (25) for the valence band, which are then solved self-consistently (SC).[37] The orientation of the wurtzite crystal, having either the A or M or off-axis planes characterized by polar and azimuthal Euler angles, can also be included in such a model.[34,35] These more elaborate models that include the internal electric fields due to SP and PZ, and also consider the wurtzite crystal orientation, build on the foundational model described, and are included with software device simulation packages.

For the GaN-VCSEL diode structure having a single $In_{0.02}Ga_{0.98}N$ quantum well grown pseudomorphically in the [0001] direction on GaN material being analyzed here, that is similar to the first room temperature, current injection GaN-VCSEL of Higuchi et al.,[24] it is appropriate to use the model presented without SP and PZ fields, to estimate the device threshold current i_t and optical output power P_o. The SP and PZ fields can be disregarded because at high carrier densities and lasing power, the built in polarization fields have been shown to be screened effectively both in theory and experiment.[37,38] Using the above theoretical model for wurtzite semiconductors such as InGaN/GaN grown on C-plane sapphire, it is possible to construct the one dimensional potential energy profile for the $In_{0.02}Ga_{0.98}N$ quantum well layer between GaN material, showing the band-edge energies defined in Eqs. (9) and (16) for the conduction and valence bands, respectively. The wurtzite $In_{0.02}Ga_{0.98}N$ layer of the quantum well is characterized by a lattice constant a_w that is larger than the lattice constant a_s of the GaN substrate layer, thereby creating a biaxial compressive strain on the $In_{0.02}Ga_{0.98}N$ according to Eq. (13) where $\varepsilon_{xx} = \varepsilon_{yy}$ will be negative. A simplification can be made however, to disregard strain in the material layers due to $In_{0.02}Ga_{0.98}N$ containing a very low indium mole fraction $x = 0.02$, thus assuming perfect lattice

matching ($a_w \approx a_s$) of the quantum well with GaN substrate. Without strain present, Eq. (7) can be used to define the conduction band-edge and Eq. (16) can be reformulated as shown in Eq. (27) to define the valence band-edge energies.

$$E_1^0 = E_v^0 + \Delta_1 + \Delta_2$$

$$E_2^0 = E_v^0 + \frac{\Delta_1 - \Delta_2}{2} + \sqrt{\left(\frac{\Delta_1 - \Delta_2}{2}\right)^2 + 2\Delta_3^2}$$

$$E_3^0 = E_v^0 + \frac{\Delta_1 - \Delta_2}{2} - \sqrt{\left(\frac{\Delta_1 - \Delta_2}{2}\right)^2 + 2\Delta_3^2}.$$
$$(27)$$

In Eq. (27), the valence band-edge energies are given by E_1^0, E_2^0 and E_3^0, where Δ_1 is the crystal field energy, Δ_2 is the spin orbit energy, Δ_3 represents a spin-orbit interaction and reference energy $E_v^0 = 0$ eV. The strain effects are not present and the earlier deformation potentials $D_1 - D_4$ in Eq. (16) which are usually determined from experimental strain-resolved exciton resonance peak data, are not needed here due to the very close lattice matching between quantum well and substrate.[39]

In bulk form, the $In_{0.02}Ga_{0.98}N$ quantum well layer has a bandgap given by Eq. (3) as $E_{g(InGaN)} = 3.357$ eV corresponding to an optical wavelength $\lambda_0 = 370$ nm for band-to-band transitions at or near room temperature. The potential energy structure for the unstrained $L_z = 10$ nm, $In_{0.02}Ga_{0.98}N$ single quantum well surrounded by GaN can be calculated using the physical parameter constants given in Table 3, by linearly interpolating the parameter values between GaN and InN for the $In_{0.02}Ga_{0.98}N$ quantum well layer.

Using the data shown in Table 3, the potential energy structure of the unstrained $In_{0.02}Ga_{0.98}N$ single quantum well layer of width $L_z = 10$ nm, surrounded by p-GaN and n-GaN is calculated in Fig. 9. Since the $In_{0.02}Ga_{0.98}N$ quantum well layer between GaN is considered to be unstrained, the deformation potentials a_{hi}, a_c, $D_1 - D_4$ and elastic stiffness constants C_{13} and C_{33} from Table 3 are not needed to calculate in Eqs. (7) and (27), the conduction and valence band-edge energies, respectively.

In Fig. 9 the band-edge energies are shown, calculated according to Eqs. (7) and (27) for an unstrained wurtzite $In_{0.02}Ga_{0.98}N$ quantum well layer of width $L_z = 10$ nm, surrounded by GaN material. The constants in Table 3, given for both InN and GaN were used for calculating band-edge energies by linear interpolation to reflect the $In_{0.02}Ga_{0.98}N$ material. In Eq. (27), E_1^0 gives the band-edge energy E_{HH}^0 shown in Fig. 9, corresponding to the heavy hole (HH) or A-type hole, E_2^0 gives E_{LH}^0 corresponding to the light hole (LH) or B-type hole and E_3^0 gives E_{CH}^0 corresponding to the crystal field split hole (CH) or C-type hole. The valence band offset energy for a wurtzite InN/GaN heterojunction grown on C-plane substrate has been reported from experiment to be $\Delta E_v = 0.58 \pm 0.08$ eV at room temperature, forming the type-I straddling configuration.[45] The band-edge discontinuity ratio of 20% for the valence band and 80% for the conduction band is suggested by the measurement of the valence band offset energy by King et al., and is relatively near in value to what others have proposed as well.[46] The valence band offset energy measured for In/GaN was used to calculate the expected valence band offset energy ΔE_v for the $In_{0.02}Ga_{0.98}N$ quantum well on GaN shown in Fig. 9, by interpolation according to Eq. (28).[33]

Table 3 Physical parameter constants for GaN and InN materials.

Parameter	GaN	InN
Lattice constant (Å)		
a	3.189[30]	3.535[30]
Energy (eV)		
E_g (300 K)	3.43[30]	0.77[30]
$\Delta_1 = \Delta_{cr}$	0.021[39]	0.041[38]
$3\Delta_2 = 3\Delta_3 = \Delta_{so}$	0.016[39]	0.001[38]
Conduction band effective masses		
m_e^z/m_0	0.20[31]	0.11[38]
m_e^t/m_0	0.18[31]	0.11[38]
Valence band effective masses		
m_{hh}^z/m_0	1.10[31]	1.58[40]
m_{lh}^z/m_0	1.10[31]	1.58[40]
m_{split}^z/m_0	0.15[31]	1.10[40]
m_{hh}^t/m_0	1.65[31]	2.06[40]
m_{lh}^t/m_0	0.15[31]	2.06[40]
m_{split}^t/m_0	1.10[31]	1.59[40]
Valence band effective mass parameters		
A_1	−6.56[31]	−9.09[41]
A_2	−0.91[31]	−0.63[41]
A_3	5.65[31]	8.46 [Eq.(15)]
A_4	−2.83[31]	−4.23 [Eq. (15)]
A_5	−3.13[31]	−4.36[41]
A_6	−4.86[31]	−6.35 [Eq. (15)]
Deformation potentials (eV)		
a_{hi} (hydrostatic interband)	−9.20[42]	−2.80[43]
a_c (hydrostatic E_c)	−4.60[40]	−1.40[40]
D_1	−1.70[40]	−1.76[44]
D_2	6.30[40]	3.43[44]
D_3	8.00 [Eq. (15)]	5.16 [Eq. (15)]
D_4	−4.00 [Eq. (15)]	−2.58 [Eq. (15)]
Elastic stiffness constants (GPA)		
C_{13}	100[43]	94[43]
C_{33}	392[43]	200[43]

Band-edge energies	
$E_{g(GaN)}$	3.43 eV
$E_{g(InGaN)}$	3.357 eV
$E_{v(InGaN)}^0$	0.0 eV
$E_{HH(InGaN)}^0$	0.026 eV
$E_{LH(InGaN)}^0$	0.019 eV
$E_{CH(InGaN)}^0$	-0.0030 eV
$E_{c(InGaN)}^0$	3.383 eV
$E_{v(GaN)}^0$	0.0 eV
$E_{HH(GaN)}^0$	0.026 eV
$E_{LH(GaN)}^0$	0.019 eV
$E_{CH(GaN)}^0$	-0.0030 eV
$E_{c(GaN)}^0$	3.456 eV
ΔE_c	0.0575 eV
ΔE_v	0.0155 eV

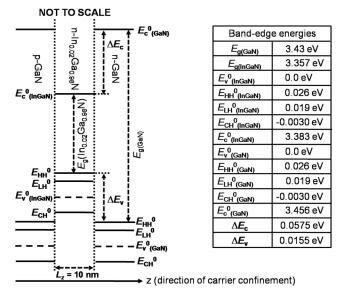**Fig. 9** Band-edge energies for the $In_{0.02}Ga_{0.98}N$ single quantum well layer between GaN.

$$E_{HH(In_xGa_{(1-x)}N)}^0 = (x)E_{HH(InN)}^0 + (1-x)E_{HH(GaN)}^0$$
$$+ B_v x(1-x)$$
$$E_{c(In_xGa_{(1-x)}N)}^0 = (x)E_{c(InN)}^0 + (1-x)E_{c(GaN)}^0$$
$$- B_c x(1-x)$$
$$B = B_c - B_v \quad B_v = 0.2B. \tag{28}$$

In Eq. (28), $E_{HH(InxGal-xN)}^0$ is the heavy hole band-edge shown in Fig. 9, expressed relative to the $E_{HH(GaN)}^0$ band-edge and thereby corresponding to the valence band offset energy ΔE_v as a function of the indium mole fraction parameter x. Thus in Eq. (28), for $x = 1$, $E_{HH(InxGal-xN)}^0 = E_{HH(InN)}^0 = \Delta E_v = 0.58$ eV. The bowing parameter B_v for the valence band is set to 20% of the bandgap bowing parameter $B = 1.01$ eV, the latter given in Table 1. For a value $x = 0.02$ corresponding to the $In_{0.02}Ga_{0.98}N$ single quantum well in Fig. 9, $E_{HH(InxGal-xN)}^0 = \Delta E_v = 0.0155$ eV as noted in the figure. For the conduction band-edge, $E_{c(InxGal-xN)}^0$ is shown in Fig. 9 and can be expressed in terms of $E_{c(InN)}^0$ and $E_{c(GaN)}^0$ which are calculated from Eq. (7) using data from Table 3. The bowing parameter $B_c = B + B_v$. In Eq. (28), the positive sign occurs in front of B_v while there is a negative sign in front of B_c for the $E_{HH(InxGal-xN)}^0$ and $E_{c(InxGal-xN)}^0$ expressions, respectively since the equations are related through the bandgap expression $E_{g(InxGal-xN)}$, the latter given in Eq. (3). The conduction band offset ΔE_c shown in Fig. 9 for the $In_{0.02}Ga_{0.98}N$ quantum well on GaN can be calculated most directly once the valence band offset $\Delta E_v = E_{HH(InxGal-xN)}^0$ has been calculated from Eq. (28), using Eq. (29).

$$\Delta E_c = E_{g(GaN)} - (E_{g(In_{0.02}Ga_{0.98}N)} + \Delta E_v). \tag{29}$$

In Eq. (29), ΔE_c is the conduction band offset energy, $E_{g(GaN)}$ is the bandgap of GaN given in Table 1,

$E_{g(\text{In}_{0.02}\text{Ga}_{0.98}\text{N})}$ is the bandgap of the $\text{In}_{0.02}\text{Ga}_{0.98}\text{N}$ quantum well calculated from Eq. (3), and ΔE_v is the valence band offset energy calculated from Eq. (28).

It becomes clear from the calculated band-edge energies and offset potentials in Fig. 9, that the unstrained $\text{In}_{0.02}\text{Ga}_{0.98}\text{N}$ single quantum well layer on GaN, is in fact not really a quantum well due to the low indium mole fraction ($x = 0.02$), resulting in a bandgap almost equal to GaN and small values for ΔE_v and ΔE_c. In fact, only the first two band-edge energies E_{HH}^0 and E_{LH}^0 in the valence band of $\text{In}_{0.02}\text{Ga}_{0.98}\text{N}$ can be considered to be confined within the potential barrier, while a nearly similar situation exists for the conduction band-edge where $\Delta E_c = 0.0575$ eV as indicated in Fig. 9. In the GaN-VCSEL device structure in Fig. 9, there will therefore exist little to no carrier confinement in the $\text{In}_{0.02}\text{Ga}_{0.98}\text{N}$ quantum well at or near room temperature.

To simplify the analysis of the GaN-VCSEL diode with $\text{In}_{0.02}\text{Ga}_{0.98}\text{N}$ single quantum well, only a single TE-mode transition in the quantum well will be evaluated namely, between the conduction subband $E_{c1}^0 \approx E_c^0$ (Fig. 9) designated C1 and the heavy hole subband $E_{\text{HH}1}^0 \approx E_{\text{HH}}^0$ (Fig. 9) designated HH1. The lowest band-edge transition energy ($E_c^0 - E_{\text{HH}}^0$) within the $\text{In}_{0.02}\text{Ga}_{0.98}\text{N}$ quantum well is the A-line or C1-HH1 transition and represents the sum of the bulk $\text{In}_{0.02}\text{Ga}_{0.98}\text{N}$ bandgap $E_{g(\text{In}_{0.02}\text{Ga}_{0.98}\text{N})}$ [calculated from Eq. (3)], the C1 quantum confined energy E_{c1}^0 and the HH1 quantum confined energy $E_{\text{HH}1}^0$. Since the C1 conduction subband energy E_{c1}^0 will be very close to E_c^0 shown in Fig. 9, and similarly the HH1 valence subband energy $E_{\text{HH}1}^0$ will be very close to E_{HH}^0 also shown in Fig. 9, the simplification is made, where $E_{c1}^0 = E_c^0$ for C1 and $E_{\text{HH}1}^0 = E_{\text{HH}}^0$ for HH1. Other transitions include $E_c^0 - E_{\text{LH}}^0$ and $E_c^0 - E_{\text{CH}}^0$ that correspond to transition energies of B-lines and C-lines, respectively.

To calculate the optical gain spectrum for the TE-mode C1-HH1 transition in the GaN-VCSEL diode quantum well, the non-Markovian optical gain with many-body effects that considers the valence band mixing is given in Eq. (30).[34,47]

$$g(\omega) = \left[1 - \exp\left(\frac{\hbar\omega - \Delta F}{k_b T}\right)\right]\sqrt{\frac{\mu_0}{\varepsilon}}\left(\frac{q^2}{m_0^2 \omega}\right)$$
$$\times \int_0^\infty dk_t \frac{k_t}{\pi L_z}|M_{nm}|^2 f_n^c(k_t)[1 - f_m^v(k_t)]L(k_t, \hbar\omega).$$

(30)

In Eq. (30), $g(\omega)$ is the optical gain, $\hbar$ is the reduced Planck constant, ω is the angular frequency, k_b is the Boltzmann constant, T is the temperature in Kelvin, ΔF is the separation between quasi-Fermi levels, μ_0 is the vacuum permeability, ε is the permittivity, q is the electron charge and m_0 is the mass of an electron. The quantity L_z is the thickness of the $\text{In}_{0.02}\text{Ga}_{0.98}\text{N}$ single quantum well, k_t is the wavevector in the quantum well plane, $|M_{nm}|^2$ represents the momentum matrix element in the single quantum well, f_n^c and f_m^v represent the Fermi functions for the conduction band and valence band states, respectively. The quantity $L(k_t, \hbar\omega)$ represents the line shape function with many-body effects that has a non-Markovian or Gaussian shape.[47] The line shape function can be Gaussian (non-Markovian) or Lorentzian (Markovian), and can account for the Coulomb interaction as well as carrier-carrier scattering either with a constant or k-dependent intraband relaxation time. The line shape function is not considered essential for estimating the threshold current i_t and optical output power P_o of the GaN-VCSEL diode from Fig. 6 with an $\text{In}_{0.02}\text{Ga}_{0.98}\text{N}$ single quantum well, the latter described in Fig. 9. A simpler model for the optical gain spectrum for the TE-mode C1-HH1 transition in the quantum well is used, that assumes a zero line width and disregards exciton effects due to Coulomb interaction between the electrons and holes, as given in Eq. (31).[48,49]

$$g(\hbar\omega) = C_0 \sum_{n,m} |I_{hm}^{en}|^2 |\hat{e} \cdot M_{nm}|^2_{(k_t=0,k_z=0)} [f_n^c(E_t = \hbar\omega - E_{hm}^{en}) - f_m^v(E_t = \hbar\omega - E_{hm}^{en})]\rho_r^{2D} H(\hbar\omega - E_{hm}^{en})$$

$$C_0 = \frac{\pi q^2}{n_r c \varepsilon_0 m_0^2 \omega}$$

$$I_{hm}^{en} = \int_{-\infty}^{\infty} dz\, \phi_n(z) g_m(z)$$

$$|\hat{x} \cdot M_{nm}|^2 = \left| -\frac{1}{\sqrt{2}} g_1 \alpha^* \langle S|p_x|X\rangle + \frac{1}{\sqrt{2}} g_2 \beta \langle S|p_x|X\rangle \right|^2 = \left| -\frac{1}{\sqrt{2}} g_4 \alpha^* \langle S|p_x|X\rangle + \frac{1}{\sqrt{2}} g_5 \beta \langle S|p_x|X\rangle \right|^2$$

$$\alpha = \frac{1}{\sqrt{2}} e^{i(\frac{3\pi}{4})} \qquad \beta = \frac{1}{\sqrt{2}} e^{i(\frac{\pi}{4})}$$

$$\langle S|p_x|X\rangle = \frac{m_0}{\hbar}\sqrt{\frac{\hbar^2}{2m_0}\left(\frac{m_0}{m_e^t} - 1\right)\frac{E_{g(\text{InGaN})}[(E_{g(\text{InGaN})} + \Delta_1 + \Delta_2)(E_{g(\text{InGaN})} + 2\Delta_2) - 2\Delta_3^2]}{(E_{g(\text{InGaN})} + \Delta_1 + \Delta_2)(E_{g(\text{InGaN})} + \Delta_2) - \Delta_3^2}}$$

$$f_n^c(E_t) = \frac{1}{1 + \exp\{[E_{c(\text{InGaN})}^0 + (m_r/m_e^t)E_t - F_c]/k_b T\}} \qquad f_m^v(E_t) = \frac{1}{1 + \exp\{[E_{\text{HH}(\text{InGaN})}^0 - (m_r/m_{hh}^t)E_t - F_v]/k_b T\}}$$

$$\rho_r^{2D} = \frac{m_r}{\pi \hbar^2 L_z} \qquad m_r = \left(\frac{1}{m_e^t} + \frac{1}{m_{hh}^t}\right)^{-1}.$$

(31)

In Eq. (31), $g(\hbar\omega)$ is the optical gain, $\hbar$ is the reduced Planck constant, ω is the angular frequency, k_b is the Boltzmann constant, T is the temperature in Kelvin, q is the electron charge, n_r is the refractive index of the GaN material, c is the speed of light, ε_0 is the permittivity in vacuum, and m_0 is the mass of an electron. The quantity I_{hm}^{en} represents the degree of overlap of the wave functions for the electrons and holes in the quantum well and $I_{hm}^{en} = \delta_{nm}$ for a symmetric, infinite quantum well, where the subscript m represents the valence subband and n represents the conduction subband. The quantities ϕ_n and g_m represent the envelope functions of the nth conduction subband and mth valence subband, respectively. It will be assumed that $|I_{hm}^{en}|^2 = 1$, signifying a perfect overlapping of the wave functions in the C1 conduction subband having a band-edge energy $E_{c1}^0 = E_c^0$, and in the HH1 valence subband having a band-edge energy $E_{HH1}^0 = E_{HH}^0$. The quantity $|\hat{e} \cdot M_{nm}|^2$ with subscripts n and m, represents the momentum matrix element in the single quantum well, and will be calculated here for the TE-mode C1-HH1 transition at the band-edges, thus $\hat{e} = \hat{x}$ or $\hat{y}$, $n = $ C1 for the conduction subband, $m = $ HH1 for the valence subband, with $k_t = (k_x^2 + k_y^2)^{0.5} = 0$ and $k_z = 0$ as indicated.[40,49] The terms α and β represent quantities that are a part of the bases functions $|1> - |6>$ for the block-diagonalized Hamiltonian matrix from Eq. (10) and are defined in Eq. (31).[40] The parameter $<S|p_x|X>$ is also defined where $E_{g(InGaN)}$ is the bandgap energy of the quantum well shown in Fig. 9, with parameters Δ_1, Δ_2 and Δ_3 having linearly interpolated values based on the data from Table 3. The quantities f_n^c and f_m^v represent the Fermi functions for the conduction band and valence band states, respectively where the subscript $n = $ C1 represents the conduction subband having band-edge energy $E_{c1}^0 = E_c^0$ and $m = $ HH1 represents the valence subband having band-edge energy $E_{HH1}^0 = E_{HH}^0$. The quantity $E_{c(InGaN)}^0 = E_{c1}^0 = E_c^0$ represents the band-edge energy of the C1 conduction subband and $E_{HH(InGaN)}^0 = E_{HH1}^0 = E_{HH}^0$ represents the band-edge energy of the HH1 valence subband, indicated in Fig. 9. The quantity E_t is defined in Eq. (31) as the difference between $\hbar\omega$ and E_{hm}^{en} where the latter represents the C1-HH1 transition energy approximated by $E_{g(InGaN)} = E_{c(InGaN)}^0 - E_{HH(InGaN)}^0 = 3.357$ eV shown in Fig. 9. The quantities F_c and F_v represent the quasi-Fermi levels for the conduction and valence bands, respectively and their separation $\Delta F = F_c - F_v$ gives an indication of the level of injection of excess electrons and holes by the optical or electrical means. The quantity ρ_r^{2D} provides the 2D joint density of states in the quantum well structure, with thickness L_z and the quantity m_r is the reduced effective mass with effective mass contributions from electrons m_e^t and heavy holes m_{hh}^t in the direction perpendicular to the [0001] or C-axis, for the C1-HH1 transition being evaluated here. In reality,

valence band mixing will occur due to the non-parabolic heavy hole (HH), light hole (LH) and split-off (CH) bands, resulting in a density of states for the valence bands that is non-step like as compared with the parabolic conduction bands. With valence band mixing due to non-parabolic bands, a more complicated expression for the density of states occurs than what is provided by ρ_r^{2D} in Eq. (31), however, valence band mixing effects will not be considered in the present analysis.[33] In addition to the optical gain spectrum evaluated here for the TE-mode C1-HH1 transition, other transitions can also occur, including the C1-LH1 and C1-CH1 transitions that contribute to the optical gain of the TE-mode, however, these transitions are not as strong as the C1-HH1 transition and are therefore not included within the analysis.[40]

To calculate the optical gain spectrum according to Eq. (31) for the TE-mode C1-HH1 transition, the envelope functions g_1, and g_2 must be calculated. It is possible to find the three analytical solutions to the valence band eigenequation Eq. (24), by formulating as shown in Eq. (32).[40]

$$H_{3x3}^U(\vec{k})\begin{bmatrix} g_1 \\ g_2 \\ g_3 \end{bmatrix} = E \begin{bmatrix} g_1 \\ g_2 \\ g_3 \end{bmatrix}$$

$$E_{HH} = (S_1 + S_2) - \frac{C_2}{3}$$

$$E_{LH} = -\frac{1}{2}(S_1 + S_2) - \frac{C_2}{3} + \frac{i\sqrt{3}}{2}(S_1 - S_2)$$

$$E_{CH} = -\frac{1}{2}(S_1 + S_2) - \frac{C_2}{3} - \frac{i\sqrt{3}}{2}(S_1 - S_2)$$

$$q = \frac{1}{3}C_1 - \frac{1}{9}C_2^2 \qquad r = \frac{1}{6}(C_1 C_2 - 3C_0) - \frac{1}{27}C_2^3$$

$$S_1 = [r + (q^3 + r^2)^{0.5}]^{0.33} \qquad S_2 = [r - (q^3 + r^2)^{0.5}]^{0.33}$$

$$C_0 = -(FG\lambda + 2K_t H_t^2 - H_t^2 G - K_t^2 \lambda - F\Delta^2 - FH_t^2)$$

$$C_1 = FG + G\lambda + F\lambda - \Delta^2 - K_t^2 - 2H_t^2$$

$$C_2 = -(F + G + \lambda). \tag{32}$$

In Eq. (32), the energy E_{HH} corresponds to the heavy hole (HH) valence band, E_{LH} corresponds to the light hole (LH) valence band and E_{CH} corresponds to the split-off hole (CH) valence band in the $In_{0.02}Ga_{0.98}N$ quantum well. To obtain the C_0, C_1 and C_2, parameter values used in calculating E_{HH}, E_{LH} and E_{CH}, the parameters F, G, λ, K_t, H_t, and Δ defined in Eq. (11) are computed without strain, using the data in Table 3, with linearly interpolated valence band parameters $A_1 - A_6$. After computing the three eigenvalues E_{HH}, E_{LH} and E_{CH}, the corresponding eigenfunctions or envelope functions g_m can also be calculated according to Eq. (33).[40]

$$\begin{bmatrix} g_1^v \\ g_2^v \\ g_3^v \end{bmatrix} = \frac{1}{D^v}\begin{bmatrix} iH_t(G - E^v) + (\Delta - iH_t)K_t \\ -iH_t K_t - (\Delta - iH_t)(F - E^v) \\ (G - E^v)(F - E^v) - K_t^2 \end{bmatrix}$$

$$D^v = \sqrt{|iH_t(G - E^v) + K_t(\Delta - iH_t)|^2 + |iH_t K_t + (\Delta - iH_t)(F - E^v)|^2 + |(G - E^v)(F - E^v) - K_t^2|^2}. \tag{33}$$

In Eq. (33) the valence band envelope functions g_1^v, g_2^v and g_3^v can be calculated where superscript v denotes HH, LH or CH bands. Thus, for calculating the gain spectrum of the TE-mode C1-HH1 transition according to Eq. (31), the envelope or eigenfunctions g_1^{HH}, g_2^{HH} and g_3^{HH} for the heavy hole band are needed and E_{HH} from Eq. (32) should therefore be substituted for E^v in Eq. (33). In Eq. (33), the parameters G, λ, K_t, H_t, and Δ defined in Eq. (11) are computed without strain, using the data in Table 3, with linearly interpolated valence band parameters $A_1 - A_6$.

The quasi-Fermi levels for the conduction band F_c and valence band F_v can be computed from Eqs. (34) and (35), respectively.[48]

$$F_c = E_{c(\text{InGaN})}^0 + (k_b T) \ln \left[\exp \left(\frac{N_n \pi \hbar^2 L_z}{m_e^t k_b T} \right) - 1 \right] \quad (34)$$

$$F_v = E_{\text{HH(InGaN)}}^0 + (k_b T) \ln \left[\exp \left(\frac{P_m \pi \hbar^2 L_z}{m_{hh}^t k_b T} \right) - 1 \right] \quad (35)$$

$$P - N_A^- = N - N_D^+.$$

In Eq. (34), $E_{c(\text{InGaN})}^0$ is the band-edge energy of the C1 conduction subband in the quantum well, k_b is the Boltzmann constant, T is the temperature in Kelvin, $\hbar$ is the reduced Planck constant, m_e^t is the electron effective mass perpendicular to the C-axis and N_n represents the electron density per unit volume in the nth conduction subband, where $n = C1$ for calculation purposes here. In Eq. (35), $E_{\text{HH(InGaN)}}^0$ is the band-edge energy of the HH1 valence subband in the quantum well, m_{hh}^t is the hole effective mass perpendicular to the C-axis and P_m represents the hole density per unit volume in the mth valence subband, where $m = HH1$ for calculation purposes here. It is assumed that at high levels of carrier injection $P \approx N$, since $P \gg N_A^-$ and $N \gg N_D^+$ here N_A^- is the ionized acceptor concentration and N_D^+ is the ionized donor concentration in the semiconductor. The expression for the quasi-Fermi level F_v in the valence band given by Eq. (35), assumes that no valence band mixing occurs due to non-parabolic valence bands, which is not exactly true.[33] It is possible to calculate the quasi-Fermi level F_v for the valence band, with mixing due to non-parabolic bands by using a computed non-step like density of states function for the valence band in the calculation of F_v, however, such valence band mixing will not be considered here.[33,48]

The threshold current i_t of the GaN-VCSEL diode can be estimated from Eq. (36).[12]

$$i_t = A_{SQW} \left(\frac{\alpha_r + \alpha_{eq}}{\alpha_{eq}} \right) \left[\left(\frac{q L_z N_{TRP}}{\eta_i \tau_r} \right) \right] \quad \alpha_r = \frac{1}{\Gamma} (\alpha_s + \alpha_m)$$

$$\alpha_m = \alpha_{m1} + \alpha_{m2} = \frac{1}{2d_r} \ln \left(\frac{1}{R_1 R_2} \right) \qquad \alpha_s = \alpha_m. \quad (36)$$

In Eq. (36), i_t represents the threshold current of the GaN-VCSEL diode, A_{SQW} is the cross sectional area of the $\text{In}_{0.02}\text{Ga}_{0.98}\text{N}$ single quantum well, q is the charge of an electron, L_z is the thickness of the well, N_{TRP} is the injected carrier concentration needed to achieve transparency in the semiconductor, η_i represents the internal quantum efficiency, and τ_r is the radiative electron-hole recombination lifetime.

The quantity α_{eq} represents the absorption coefficient at thermal equilibrium, α_r is the total absorption loss coefficient comprised of the reflection loss coefficient α_m, and the loss coefficient due to scattering and free carrier absorption α_s. It is assumed here that $\alpha_s = \alpha_m$. The quantities α_{m1} and α_{m2} are reflection loss coefficients of the front-side and back-side mirrors, respectively of the resonator. The confinement factor Γ represents the fraction of the optical energy within the active region of the GaN-VCSEL diode. The quantity, d_r represents the length of the resonator cavity, R_1 is the reflectance of the front-side AlN/GaN DBR mirror, and R_2 is the reflectance of the back-side $\text{SiO}_2/\text{HfO}_2$ DBR mirror.

The optical output power P_o of the GaN-VCSEL diode can be estimated from Eq. (37).[12]

$$P_o = h\nu\eta_e\eta_i \frac{i_d - i_t}{q} \quad \eta_e = \frac{\alpha_{m1}}{\alpha_r} \qquad \alpha_{m1} = \frac{1}{2d_r} \ln \left(\frac{1}{R_1} \right). \quad (37)$$

In Eq. (37), P_o is the optical output power of the GaN-VCSEL diode, h is the Planck constant, ν is the frequency corresponding to the lasing wavelength $\lambda_0 = 370$ nm, q represents the charge of an electron, i_d is the injected drive current, i_t is the threshold current, η_i is the internal quantum efficiency and η_e is the external quantum efficiency that is calculated based on the assumption that light is only transmitted out through the front-side AlN/GaN DBR mirror having a reflectance R_1. The quantity α_{m1} is the reflection loss coefficient of the front-side mirror, α_r is the total absorption loss coefficient defined in Eq. (36) with d_r being the length of the resonator cavity.

Using Eqs. (32)–(35) it becomes possible to calculate the zero line width optical gain spectrum given by Eq. (31) for the TE-mode C1-HH1 transition in the $\text{In}_{0.02}\text{Ga}_{0.98}\text{N}$ single quantum well of the GaN-VCSEL diode grown on wurtzite C-plane material that will yield the value for the injected carrier concentration N_{TRP}, needed to achieve transparency in the semiconductor. The transparency carrier concentration N_{TRP}, is used in Eq. (36) to estimate the threshold current i_t of the GaN-VCSEL diode. Subsequently, Eq. (37) can be used to estimate the GaN-VCSEL diode optical output power P_o as a function of the drive current i_d.

In Table 4, parameter values are provided for calculating the estimated optical gain spectrum and optical output power as a function of drive current for the TE-mode C1-HH1 transition in the $\text{In}_{0.02}\text{Ga}_{0.98}\text{N}$ single quantum well of the GaN-VCSEL diode grown on wurtzite C-plane material.

The data from Table 4, is used to calculate the zero line width optical gain spectrum according to Eq. (31) in Fig. 10, yielding the value of the injected carrier concentration N_{TRP}, needed to achieve transparency in the semiconductor. The transparency injected carrier concentration N_{TRP} listed in Table 4 and shown in Fig. 10, can be used to compute the estimated GaN-VCSEL threshold current i_t according to Eq. (36).

In Fig. 11, the estimated optical output power P_o is shown as a function of the drive current i_d calculated using Eq. (37). A laser diode drive current $i_d = 10.7$ mA, corresponding to $N = 1.6 \times 10^{19}$ cm^{-3} is sufficient to generate an optical output power $P_o = 4$ mW for the GaN-VCSEL diode with $\text{In}_{0.02}\text{Ga}_{0.98}\text{N}$ single quantum well on wurtzite C-plane substrate, having the geometry and characteristics described

Table 4 GaN-VCSEL diode parameters.

Parameter	Value
Operating temperature	$T = 243$ K
Design wavelength	$\lambda_0 = 370$ nm
Active region single quantum well (SQW) composition	$In_{0.02}Ga_{0.98}N$
Active region bandgap	$E_{g(InGaN)} = 3.357$ eV
Optical transition in SQW	C1-HH1 (TE-mode)
Electron mass	$m_0 = 9.109 \times 10^{-31}$ kg
Electron effective mass in SQW (transverse)	$m_e^t = 0.18 m_0$ kg
Heavy hole effective mass in SQW (transverse)	$m_{hh}^t = 1.66 m_0$ kg
Quantum well thickness	$L_z = 10$ nm
Quantum well area	$A_{SQW} = 1.63 \times 10^{-7}$ cm^2
Resonator cavity length	$d_r = 1.195 \times 10^{-4}$ cm
Front-side AlN/GaN DBR mirror reflectance	$R_1 = 0.9979$[17]
Back-side SiO$_2$/HfO$_2$ mirror reflectance	$R_2 = 0.9999$[17]
Absorption coefficient (GaN) at thermal equilibrium ($h\nu = 3.4$ eV, 293 K)	$\alpha_{eq} = 14.38 \times 10^3$ cm^{-1}[50]
Confinement factor of the optical energy	$\Gamma = 1$
Refractive index (GaN) at design wavelength $\lambda_0 = 370$ nm	$n_r = 2.56$[10]
Internal quantum efficiency ($In_{0.02}Ga_{0.98}N$)	$\eta_i = 0.3$[51]
Radiative electron-hole recombination lifetime ($In_{0.02}Ga_{0.98}N$) 300 K	$\tau_r = 0.13 \times 10^{-9}$ sec[52]
Transparency carrier concentration	$N_{TRP} = 2.75 \times 10^{18}$ cm^{-3}

in Figs. 6 and 9 and Table 4. The estimated threshold current $i_t = 1.85$ mA and optical output power P_o of the GaN-VCSEL diode with $In_{0.02}Ga_{0.98}N$ single quantum well in the emitter-detector pixel, matches closely the measured threshold current and optical output power of the first room temperature, electrical injection GaN-VCSEL diodes developed by Higuchi et al. and Omae et al. on C-plane sapphire and on native GaN substrate, respectively.[24,25] The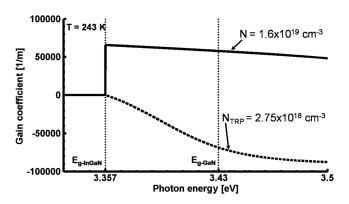 GaN-VCSEL device of Higuchi et al. had a threshold current $i_t = 7$ mA with threshold voltage of 4.3 V and an optical output power $P_o = 0.14$ mW with a drive current $i_d = 12$ mA. The GaN-VCSEL device of Omae et al. had a threshold current $i_t = 8$ mA with threshold voltage of 4.3 V and an optical output power $P_o = 0.62$ mW with a drive current $i_d = 24$ mA. Development of GaN-VCSEL diodes using more advanced designs with multiple quantum
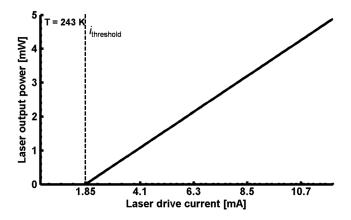

Fig. 10 Laser gain coefficient (solid curve) corresponds to a drive current $i_d = 10.7$ mA and output power $P_o = 4$ mW.

Fig. 11 Laser optical output power as a function of the drive current. Threshold current $i_t = 1.85$ mA.

wells and improved epitaxial growing methods that reduce material defects, will likely lead to further improvement in the optical output power from such devices, similar to the edge-emitting laser diodes that first started being developed two decades ago and presently achieve optical output powers of 50 to 100 mW or more.[38]

If the readout integrated control circuit for the emitter-detector FPA will be implemented in a TSMC 0.25 μm process for example, then the drive transistor can be readily sized to the appropriate width to source a current $i_d = 10.7$ mA that will generate an optical output power $P_o = 4$ mW while still allowing the pixel circuit to fit into a 27 μm square. It will be shown through further calculations in Sec. 4 that the levels of optical power generated per pixel by the VCSEL diodes will be sufficient to support active detection mode with high sensitivity for the emitter-detector based FPA.

3.2 Silicon Avalanche Photodiode Design

The design of the crystallographically etched, wide dynamic range silicon mesa avalanche photodiode, capable of operating in dual linear and Geiger-mode has been described previously.[5,8] It has been shown that the silicon mesa APD will operate with high quantum efficiency and the array will achieve 100% sensitive-area-fill-factor due to the antireflective layer between the sapphire and silicon and due to the spherical sapphire microlens. In the conventional silicon mesa APD, the microlens focuses optical rays under full height of the silicon mesa and away from the mesa sidewalls that have a reduced height as well as away from the optical dead space between pixels where the silicon has been etched, to enable low resistance anode contacts and direct pixel-to-pixel optical crosstalk isolation. In the present emitter-detector pixel design, the microlens curvature has been optimized to relay the laser beam as well as focus optical returns into the detector silicon. Accomodating the GaN-VCSEL diode removes more silicon from each pixel, thereby reducing the APD detector quantum efficiency. It is possible to calculate the emitter-detector pixel quantum efficiency for light at normal incidence to the back-illuminated sapphire plane, using Monte Carlo integration. Figure 12, shows the 3D model of the silicon mesa APD pixel of 6 μm height with etched laser diode cavity and DBR trench. Light rays or
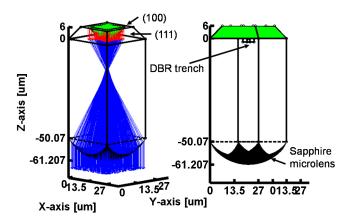

Fig. 12 Geometry of the 27 μm silicon APD detector mesa with laser diode cavity showing 3D ray tracing for light rays normally incident to the sapphire plane.
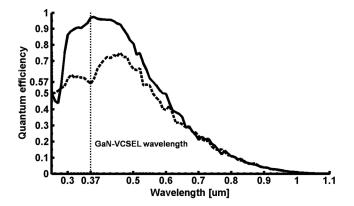

Fig. 13 Quantum efficiency of the emitter-detector pixel using MgF$_2$(82 nm)-Sapphire-AlN(82 nm)-Si (dashed line) and MgF$_2$ (70 nm)-Sapphire-AlN/SiN$_{0.62}$(48/22 nm)-Si (thick solid line) substrates.

k-vectors of TE waves are randomly generated and launched at normal incidence to the sapphire wafer plane but not to the curved surface of the microlens.

Using the Monte Carlo integration approach, it is possible to calculate the average distance that an optical k-vector will propagate in the silicon APD detector mesa as a function of wavelength. If the k-vector encounters the front-side DBR, it is considered lost. The distance travelled by the k-vector in the silicon mesa is calculated from knowing the equations of the bounding planes formed by the (111) and (100) crystal planes on the exteriors and top of the pixel, respectively. In Fig. 13, it is evident that although the quantum efficiency of the APD detector pixel is sacrificed for longer wavelengths by etching the laser diode cavity in the silicon, the quantum efficiency is less adversely affected in the visible and ultra-violet where the focal plane is in fact designed to operate. At the laser design wavelength $\lambda_0 = 370$ nm, the detector quantum efficiency is calculated to be 97% for very high transmittance, back-illuminated Si-(AlN/a-SiN$_{0.62}$)-sapphire-(MgF$_2$) wafer substrate introduced in Fig. 3. The pronounced curvature of the optimal microlens for the emitter-detector pixel is evident in the scale rendering in Fig. 12.

4 Sensitivity of the Active Emitter-Detector Pixel

The sensitivity of the emitter-detector pixel operating in an active mode is calculated in this section for the ideal case of perfectly diffuse reflection of the active laser signal from an object with a Lambertian surface. It will be shown that the emitter-detector pixel design presented here using very high transmittance, back-illuminated Si-(AlN/a-SiN$_{0.62}$)-sapphire-(MgF$_2$) wafer substrate is capable of operating with high sensitivity in an active mode. The emitter-detector pixel operates as a self-contained optical radar element consisting of the emitter-detector device and its associated control circuit shown in Fig. 14.

The emitter-detector pixels are controlled using the waveforms shown in Fig. 15, that may be applied either in unison or sequentially to each pixel in an example 1024 × 1024 element array with appropriate time delay between the pixels.

The sensitivity calculation yields a result that is identical whether the pixel lasers in the focal plane are triggered in unison and the optical returns are collected by arming all APDs synchronously at the time of the expected returns, or if the lasers and corresponding APDs of the pixels are
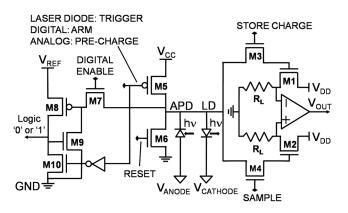
Fig. 14 Emitter-detector pixel control circuit showing common electrical connection between the laser diode anode and 27 μm wide dynamic range silicon mesa APD.

scanned sequentially for the entire 1024×1024 array. Triggering all the laser diodes in unison and collecting the optical returns using Geiger-mode for the APDs is beneficial for rapidly measuring the range of objects in a scene. The potential drawback of triggering all laser diodes in the array simultaneously is the large expected level of heat dissipation, especially at high frame rates. Triggering the lasers and detecting their returns in sequential order is also possible and far more economical in terms of power dissipation, although it is also far slower since all 1024×1024 pixels must be electronically scanned.

In the emitter-detector pixel, transistor M5 in Fig. 14 must be sized to be capable of sourcing a large current required to forward bias the GaN-VCSEL diode. The electrical connection of the GaN-VCSEL diode anode and silicon APD cathode shown in Fig. 14, is enabled by close matching between the forward turn-on voltage of the wide bandgap GaN-VCSEL diode and the 4 to 5 V overbias voltage required for Geiger-mode operation of the silicon APD.[24,25] Proper control of the APD common anode terminal and laser diode common cathode terminal by the CMOS readout integrated circuit (ROIC), determines if activation of p-channel transistor M5 triggers the pixel laser diode to emit or alternatively, arms the silicon APD for detection. The electrical architecture of the ROIC provides maximum flexibility for FPA operation. If the common cathode terminal of the laser diodes is set to $V_{CC} \approx 4$–5 V thereby disabling the laser diodes, the FPA can be used to detect optical signals
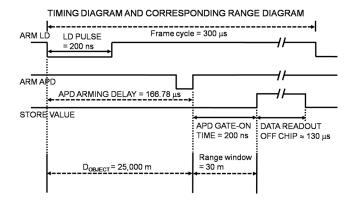
in a passive mode over a wide dynamic range in linear or Geiger-mode. For active mode operation, the ROIC architecture supports triggering the lasers of the focal plane pixels either in unison or in sequential order. To trigger the lasers, the common cathode terminal is set to ground (0 V) and the APDs are disabled by setting the common anode to ground (0 V).

The timing example in Fig. 15 assumes that the range of interest in a scene is located at a distance $D_{OBJECT} = 25,000$ m, and the depth or range window beyond the object distance is 30 m. The scenario requires the gate-on time interval of the Geiger-mode APD to be set to $T_{APD-ON} = 200$ ns corresponding to the maximum return time of flight for photons covering the full return trip of the 30 m range window. The time delay from triggering the VCSEL pulse to arming the APD is set to $T_{ARM-DELAY} = 166.78$ μs corresponding to the return time of flight for photons to an object distance $D_{OBJECT} = 25,000$ m. An optimal duration of the laser pulse equals the gate-on time interval of the Geiger-mode APD, $T_{LD-ON} = T_{APD-ON} = 200$ ns. This can be understood by visualizing how an object located at different depths in the 30 m range window affects the active laser signal returns collected by the APD. It can be understood from Fig. 15, that when the reflecting Lambertian surface is located exactly at the front of the range window at $D_{OBJECT} = 25,000$ m, the laser pulse reflection occurs during the entire gate-on time interval (T_{APD-ON}) of the APD since the duration of the laser pulse equals that of the gate-on time interval, $T_{LD-ON} = T_{APD-ON}$. If the peak power of the laser is $P_o = 4$ mW at a drive current $i_d = 10.7$ mA as seen in Fig. 11, then although the average power of the laser is much lower due to a reduced on-state duty cycle, the effective CW laser power reflected by the Lambertian surface is still 4 mW, since the APD is gated on coincident with laser diode optical returns. If the Lambertian surface is located at a distance midway inside the range window, at $D_{OBJECT} = 25,015$ m, the laser pulse reflection occurs only during half of the 200 ns gate-on interval of the APD, so the effective CW power of the Lambertian source is reduced in half from $P_o = 4$ mW to $P_o = 2$ mW. The active signal returns to the APD detector from the Lambertian surface are therefore maximized as the surface advances from the back ($D_{OBJECT} = 25,030$ m) toward the front ($D_{OBJECT} = 25,000$ m) of the range window.

4.1 Signal-to-Noise Ratio of the Emitter-Detector Pixel in Active Detection Mode

The sensitivity or signal-to-noise ratio (SNR) of the emitter-detector pixel operating in an active mode is calculated here for the ideal case of perfectly diffuse reflection of the active laser signal from an object with a Lambertian surface. The compact, 27 μm emitter-detector pixel for high resolution passive and active imaging arrays consisting of a high quantum efficiency silicon APD and GaN-VCSEL diode, can be shown to be capable of operating with high sensitivity in an active detection mode. The high quantum efficiency design of the 27 μm mesa APD detector at the laser wavelength $\lambda_0 = 370$ nm, enabled by the very high transmittance Si-(AlN/a-SiN$_{0.62}$)-sapphire substrate with $\lambda/4$-MgF$_2$ back-side antireflective layer, is the key element for maximizing the sensitivity of the photonic device. The previously calculated value of the laser peak optical power output

Fig. 15 Example timing diagram and corresponding range diagram for the emitter-detector pixel and focal plane array operation in active mode.

$P_{o\text{-PEAK}} = 4$ mW at a drive current of $i_d = 10.7$ mA, can be used in the calculation of sensitivity for the emitter-detector pixel, fabricated on the novel substrate with AlN/a-SiN$_{0.62}$ antireflective bilayer.[6] The effective optical output power of the GaN-VCSEL for calculating the signal-to-noise ratio will be half of the peak output or $P_{o\text{-SNR}} = 2$ mW assuming the object being actively imaged is located at a distance midway inside the range window and therefore, laser pulse reflection occurs only during half of the APD gate-on time interval $T_{\text{APD-ON}} = 200$ ns. Further losses in the laser diode optical power will occur due to atmospheric absorption and scattering, however, such signal losses will not be considered, although they could be readily included in the subsequent mathematical analysis of the emitter-detector pixel signal-to-noise ratio.

In active mode, the emitter-detector pixel signal-to-noise ratio for the Geiger-mode mesa APD optical receiver from Fig. 1 is calculated using the expression given in Eq. (38).[8]

$$\text{SNR}_{\text{APD–Geigermode–receiver}} = \frac{\langle i_p(t) \rangle^2}{\sigma_{i_p}^2 + \sigma_{i_D}^2}. \tag{38}$$

The average APD photocurrent $<i_p(t)>$ shown squared in the numerator of Eq. (38), represents the signal. In the denominator σ_{ip}^2 is the photoelectron noise and σ_{iD}^2 is the dark current noise. The APD optical receiver operates in digital Geiger-mode with direct photon-to-digital conversion in the pixel, thus eliminating the electronic readout noise contribution from the denominator of Eq. (38). The signal $<i_p(t)>^2$ in the numerator of Eq. (38) is calculated by assuming that the surface area illuminated by each VCSEL diode is a Lambertian source emitting into a full 2π sr hemisphere. The power emitted into the hemisphere is given by Lambert's law in Eq. (39).[53]

$$P_o = \int_{A,\Omega} dP = BA \int_{\theta=0}^{\theta=\pi/2} \cos\theta d\Omega = BA_{\text{SPOT}}\pi. \tag{39}$$

In Eq. (39), B represents the radiance which is conserved during propagation and A_{SPOT} is the area of the laser spot projected onto the Lambertian surface that in turn forms the Lambertian source. Assuming the Lambertian source is located on-axis with the camera lens and corresponding detector, the power P_0 at the camera lens and pixel, whose laser illuminated the area on the scene conjugated back to the pixel, is given by Eq. (40).

$$P_0 = BA_{\text{CAMERA-LENS}}\Omega_{\text{SPOT}}. \tag{40}$$

In Eq. (40) the solid angle Ω_{SPOT} is subtended by the area A_{SPOT} of the Lambertian source at the camera lens, the latter having an area $A_{\text{CAMERA-LENS}}$, and is given as $\Omega_{\text{SPOT}} = \pi(\theta_{\text{SPOT}})^2$ sr where $\theta_{\text{SPOT}} = \arctan((D_{\text{SPOT}}/2)/D_{\text{OBJECT}})$. In calculating θ_{SPOT} the diameter of the circular laser spot projected onto the Lambertian surface is designated as D_{SPOT} and D_{OBJECT} is the distance of the object in the scene from the camera lens as shown in Fig. 2. The mean APD detector photocurrent in the numerator of Eq. (38) is calculated according to Eq. (41).

$$\bar{i}_p = \eta G q \Phi. \tag{41}$$

In Eq. (41), the quantity η represents the APD detector quantum efficiency and depends on the optical wavelength, while G is the average internal avalanche gain of the APD, q is the charge of a single electron, and Φ represents the incident photon flux. The APD photocurrent variance σ_{ip}^2 or photocurrent noise is calculated according to Eq. (42) and the dark current variance σ_{iD}^2 or dark current noise is calculated according to Eq. (43). The detailed derivations of the expressions for the photocurrent noise and dark current noise given in Eqs. (42) and (43), respectively were performed in Ref. 8.

$$\sigma_{i_p}^2 = 2T\eta_{\text{abs.}}\Phi q^2 B(F_G\langle G\rangle^2 F_\beta\langle\beta\rangle^2 + F_\gamma\langle\gamma\rangle^2 + F_{ag}\langle G\rangle\langle\beta\rangle\langle\gamma\rangle) - T^2\eta_{\text{abs.}}^2 q^2\Phi^2\langle G\rangle\langle\beta\rangle\langle\gamma\rangle \tag{42}$$

$$\sigma_{i_D}^2 = 2\Phi_e q^2 B(F_G F_a\langle G\rangle^2\langle\eta_a\rangle^2 + F_g\langle\eta_g\rangle^2 + F_{ag}\langle G\rangle\langle\eta_a\rangle\langle\eta_g\rangle) - \Phi_e^2 q^2\langle\eta_a\rangle\langle\eta_g\rangle\langle G\rangle. \tag{43}$$

In Eq. (42), T represents the optical power transmittance into the device, η_{abs} represents the absorption efficiency of light in the silicon, Φ represents the incident photon flux, q is the charge of a single electron and B is the bandwidth. The quantities G, β and γ are all random variables where G describes the avalanche gain and parameters β and γ describe the probability of a photogenerated electron being collected in the active part of the device and multiplied or collected by the guard diode and not multiplied, respectively. The symbols F_G, F_β, F_γ, and F_{ag} describe the excess noise factors associated with G, β, γ, and $\beta\gamma$, respectively. In Eq. (43), Φ_e describes the average number of thermally generated electrons per second, q is the charge of an electron and B is the bandwidth. The quantities G, η_a, η_g are random variables where G describes the avalanche gain, while η_a describes the probability of a thermally generated electron being collected in the active region and therefore being multiplied in the APD, and η_g describes the probability of a thermally generated electron being collected by the guard diode and therefore not being multiplied. The symbols F_G, F_a, F_g, and F_{ag} describe the excess noise factors associated with G, η_a, η_g and $\eta_a\eta_g$, respectively. The parameters required to calculate the signal-to-noise ratio according to Eq. (38), of the 27 μm emitter-detector pixel of Fig. 1 illuminating a Lambertian surface, are given in Table 5.

The signal-to-noise ratio of the emitter-detector pixel operating in active mode is calculated as a function of object distance using the parameters from Table 5 with values recalculated when applicable. In Fig. 16, the emitter-detector pixel attains SNR = 1 at an object distance $D_{\text{OBJECT}} \approx$ 27,500 m and frame rate of 3222 s^{-1}. Although this result does not consider optical losses from atmospheric scattering or absorption at non-ideal Lambertian surfaces, it provides a good estimate of the expected device performance.

It is evident in Fig. 16 that the novel very high transmittance, back-illuminated Si-(AlN/a-SiN$_{0.62}$)-sapphire-(MgF$_2$) substrate with optimally tuned thickness of the antireflective layers, allows nearly 100% of the incident radiation at the laser wavelength $\lambda_0 = 370$ nm to be transmitted into the APD device silicon, thereby yielding nearly 100% APD detector quantum efficiency at the laser wavelength. In contrast to the Si-(AlN/a-SiN$_{0.62}$)-sapphire, the Si-(AlN)-sapphire substrate with $\lambda/4$-MgF$_2$ back-side

Table 5 Sensitivity calculation parameters.

Parameter	Value
Emitter-detector FPA temperature	$T = 243$ K
APD array size	1024×1024 pixels
APD pixel size	$a = 27$ μm
APD mesa pixel height	$h = 6$ μm
Microlens	Sapphire microlens
Camera lens focal length	$F = 0.21$ m
Camera focal ratio	$f/\# = 2.7$
$A_{\text{CAMERA LENS}}$	0.00477 m^2
GaN-VCSEL diode effective power	$P_{o\text{-SNR}} = 2$ mW
A_{SPOT} (at $D_{\text{OBJECT}} = 25{,}000$ m)	7.938 m^2
Ω_{SPOT} (at $D_{\text{OBJECT}} = 25{,}000$ m)	1.270×10^{-8} sr
Minority carrier lifetime τ_n in APD silicon	$\tau_n = 100$ μsec[54]
APD gate on time $T_{\text{APD-ON}}$	$T_{\text{APD-ON}} = 200$ ns
APD integration time T_{INT}	$T_{\text{INT}} = 1/2B$

antireflective layer only transmits 57% of the incident radiation into silicon at the laser wavelength. The quantum efficiency of the 27 μm emitter-detector pixel with etched laser diode cavity has a reduced quantum efficiency for the visible and near infrared wavelengths compared to a silicon mesa detector pixel without an etched cavity for the laser diode.[5,8] At the GaN-VCSEL diode wavelength of emission however, the sapphire microlens helps to focus light into the APD silicon and away from the crystallographically etched laser diode cavity, thereby preserving high detector quantum efficiency at the laser wavelength. The Si-(AlN/a-SiN$_{0.62}$)-sapphire-(MgF$_2$) substrate enables nearly two times as much light to be transmitted into the APD detector at the laser wavelength $\lambda_0 = 370$ nm compared to Si-(AlN)-sapphire-(MgF$_2$), thereby improving the unity SNR threshold of the 27 μm emitter-detector pixel to a maximum possible
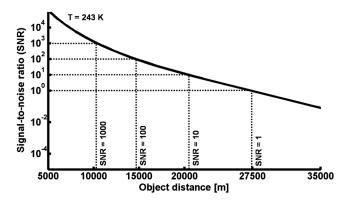

Fig. 16 Active mode sensitivity of 27 μm emitter-detector pixel using MgF$_2$(70 nm)-Sapphire-AlN/SiN$_{0.62}$(48/22 nm)-Si substrate.

range of 27,500 m. The improvement in the detection range of the optical radar pixel photonic device can be regarded as significant. High overall sensitivity is achieved by the emitter-detector pixel with SNR = 10 at $D_{\text{OBJECT}} \approx$ 20 km, SNR = 100 at $D_{\text{OBJECT}} \approx 15$ km and SNR = 1000 at $D_{\text{OBJECT}} \approx 10$ km. An enhancement in the optical output power of the GaN-VCSEL diode emitter, can lead to greater range sensitivity for the active mode APD emitter-detector pixel.

5 Application of the Active Emitter-Detector Pixel

It is possible to envision applications for the emitter-detector pixel based APD focal plane array in science and industry, however, the most intriguing possible use occurs in the medical fields of AIDS and cancer research. The progress in research on green fluorescent proteins (GFPs) has allowed the human immunodeficiency virus (HIV) to be tagged and made to fluoresce so it becomes visible/identifiable using optical means.[55–57] This can allow the development of a compact, battery powered, and wearable medical device, containing an emitter-detector pixel based APD-FPA of the type described in this paper, that screens the cells in a patient's blood on a continuous basis, identifying the HIV occupied cells from their fluorescence and destroying them in real time with the built in coherent light sources to prevent the cells from being exploited by HIV for replication, thereby actively aiding the immune system in fighting the disease. Analogously to screening cells for HIV presence, the same medical device with emitter-detector FPA can be optimized to identify misformed cancer cells using image processing in software, and to neutralize them with coherent laser light from the pixels. The compact, active mode imager of this design study represents an enabling technology for such an application because larger systems, with lasers physically separate and not directly integrated with highly sensitive APD detectors in the imaging focal plane array would be too bulky and therefore not wearable by a patient. In contrast, the novel solid-state emitter-detector FPA architecture, enables a portable and wearable device to screen the patient's cells in the blood on a 24 hour basis, to overcome the rapid replication rate of HIV with ensuing destruction of the key T-helper or CD4 immune cells after just one day on average, once HIV replication in a CD4 host cell has commenced.[58] The healthy count of CD4 cells in blood ranges between 1000 and 1200/microliter and the typical volume of blood in the human organism is 2.8 to 3.8 liters. The total number of CD4 cells that must be screened therefore will be approximately 4,560,000,000 cells given by the product of 1200 cells/μl × 3,800,000 μl. For a very high frame rate APD-FPA camera such as the one presented here, it should be possible to screen all of the cells in the blood in less than three hours.[59,60]

To add clarification, the active emitter-detector FPA imaging device would have to be used in conjunction with medication taken by a patient that affixes fluorescent proteins to newly manufactured HIV virus *in vivo*, to make it recognizable for the active emitter-detector FPA imager. Such medication does not yet exist, but could likely be developed using techniques similar to ones used to tag the HIV virus *ex vivo* with GFP.[57] This method, if realized successfully would not constitute a cure for AIDS, but could become a lower cost treatment alternative to expensive antiretroviral

drugs that can have many negative side effects and are used currently to treat the disease.

6 Concluding Remarks

It has been shown through detailed calculation and analysis means that a novel Si-$(AlN/a$-$SiN_{0.62})$-sapphire semiconductor substrate with $\lambda/4$-MgF_2 back-side antireflective layer enables the design of a 27 μm emitter-detector pixel for high resolution passive and active imaging arrays, having maximum sensitivity in the active detection mode for a given laser emitter power output. Applications for such a dual mode passive and active focal plane array imager are manifold, in particular for the medical fields of cancer and AIDS research. One might envision a biomedical role for the emitter-detector FPA in a compact, active blood filtration system where cells in the blood are optically screened by the sensor during filtration, using conventional passive imaging to determine if they are healthy or diseased. If the cell in the image collected by the sensor is determined to be diseased, the pixels in the FPA which are spatially conjugated to the area in the scene bounding the diseased cell can be switched electrically from a detecting mode, to emit UV laser radiation directly at the corresponding spatially conjugated area where the diseased cell exists to disable it. Scientific applications for the high sensitivity emitter-detector FPA imager include fiber based and free space optical communications, quantum optics research and environmental remote sensing. Industrial applications include compact optical radar for collision avoidance systems in air and on the ground. The design of the compact, high sensitivity emitter-detector pixel represents a novel and enabling photonic device technology with many important potential applications for the medical, scientific and industrial fields.

References

1. H. M. Manasevit and W. J. Simpson, "Single-crystal silicon on a sapphire substrate," *J. Appl. Phys.* **35**(4), 1349–1351 (1964).
2. S. S. Lau et al., "Improvement of crystalline quality of epitaxial silicon layers by ion-implantation techniques," *Appl. Phys. Lett.* **34**(1), 76–78 (1979).
3. G. P. Imthurn et al., "Bonded silicon-on-sapphire wafers and devices," *J. Appl. Phys.* **72**(6), 2526–2527 (1992).
4. T. Shibata et al., "AlN epitaxial growth on off-angle *R*-plane sapphire substrates by MOCVD," *J. Crystal Growth* **229**(1), 63–68 (2001).
5. A. G. Stern and D. C. Cole, "Design of a back-illuminated, crystallographically etched, silicon-on-sapphire avalanche photodiode with monolithically integrated microlens, for dual-mode passive & active imaging arrays," *Proc. SPIE* **7153**, 71530Z (2008).
6. A. G. Stern, "Design of high quantum efficiency and high resolution, Si/SiGe avalanche photodiode focal plane arrays using novel, back-illuminated, silicon-on-sapphire substrates," in J. W. Park, ed., *Photodiodes—World Activities in 2011*, ISBN: 978-953-307-530-3, InTech publisher, Vienna, pp. 267–312 (2011).
7. H. Seidel et al., "Anisotropic etching of crystalline silicon in alkaline solutions," *J. Electrochem. Soc.* **137**(11), 3612–3625 (1990).
8. A. G. Stern and D. C. Cole, "High-sensitivity, wide-dynamic-range avalanche photodiode pixel design for large-scale imaging arrays," *J. Electron. Imag.* **19**(2), 021102 (2010).
9. S. H. Park et al., "Refractive sapphire microlenses fabricated by chlorine-based inductively coupled plasma etching," *J. Appl. Opt.* **40**(22), 3698–3702 (2001).
10. Ü. Ozgür et al., "Systematic measurement of $Al_xGa_{1-x}N$ refractive indices," *Appl. Phys. Lett.* **79**(25), 4103–4105 (2001).
11. J. G. E. Gardeniers, H. A. C. Tilmans, and C. C. G. Visser, "LPCVD silicon-rich silicon nitride films for applications in micromechanics, studied with statistical experimental design," *J. Vac. Sci. Tech. A* **14**(5), 2879–2892 (1996).
12. B. E. A. Saleh and M. C. Teich, *Fundamentals of Photonics*, John Wiley & Sons, New York, pp. 246–253, 755, 789 (2007).
13. H. M. Ng, T. D. Moustakas, and N. G. Chu, "High reflectivity and broad bandwidth AlN/GaN distributed Bragg reflectors grown by molecular-beam epitaxy," *Appl. Phys. Lett.* **76**(20), 2818–2820 (2000).
14. H. H. Yao et al., "MOCVD growth of AlN/GaN DBR structures under various ambient conditions," *J. Cryst. Growth* **262**(1–4), 151–156 (2004).
15. T. Zhu et al., "Nonpolar GaN-based microcavity using AlN/GaN distributed Bragg reflector," *Appl. Phys. Lett.* **92**(6), 061114 (2008).
16. V. K. Gupta et al., "Selective area growth of GaN using gas source molecular beam epitaxy," *J. Electron. Mater.* **29**(3), 322–324 (2000).
17. A. G. Stern, "Design of a silicon avalanche photodiode pixel with integrated laser diode using back-illuminated, crystallographically etched, silicon-on-sapphire with monolithically integrated microlens, for dual-mode passive and active imaging arrays," *Proc. SPIE* **7780**, 778011 (2010).
18. J. K. Sheu et al., "InGaN light-emitting diodes with oblique sidewall facets formed by selective growth on SiO_2 patterned GaN film," *Opt. Express* **18**(S4) A562–A567 (2010).
19. S. Cihangir and S. Kwan, "Characterization of indium and solder bump bonding for pixel detectors," *Nucl. Instrum. Methods A* **476**(3), 670–675 (2002).
20. S. H. Park et al., "Room-temperature GaN vertical-cavity surface-emitting laser operation in an extended cavity scheme," *Appl. Phys. Lett.* **83**(11), 2121–2123 (2003).
21. H. Zhou et al., "Near ultraviolet optically pumped vertical cavity laser," *Electron. Lett.* **36**(21), 1777–1779 (2000).
22. C. C. Kao et al., "Fabrication and performance of blue GaN-based vertical-cavity surface emitting laser employing AlN/GaN and Ta_2O_5/SiO_2 distributed Bragg reflector," *Appl. Phys. Lett.* **87**(8), 081105 (2005).
23. T. C. Lu et al., "CW lasing of current injection blue GaN-based vertical cavity surface emitting laser," *Appl. Phys. Lett.* **92**(14), 141102–1411023 (2008).
24. Y. Higuchi et al., "Room-temperature CW lasing of a GaN-based vertical-cavity surface-emitting laser by current injection," *Appl. Phys. Express* **1**(12), 121102 (2008).
25. K. Omae et al., "Improvement in lasing characteristics of GaN-based vertical-cavity surface-emitting lasers fabricated using GaN substrate," *Appl. Phys. Express* **2**(5), 052101 (2009).
26. S. Nakamura et al., "Subband emissions of InGaN multi-quantum-well laser diodes under room-temperature continuous wave operation," *Appl. Phys. Lett.* **70**(20), 2753–2755 (1997).
27. S. Nakamura, "InGaN-based laser diodes," *Annu. Rev. Mater. Sci.* **28**, 125–152 (1998).
28. C. Erlick et al., "Atmospheric transmission in the ultraviolet and visible: Aerosols in cloudy atmospheres," *J. Geophys. Res.* **103**(D24), 31,541–31,556 (1998).
29. L. Wang, "Measuring optical absorption coefficient of pure water in UV using the integrating cavity absorption meter," Ph.D. Dissertation Texas A&M University (2008).
30. T. Kuykendall, "Complete composition tunability of InGaN nanowires using a combinational approach," *Nat. Mater. Lett.* **6**(12), 951–956 (2007).
31. M. Suzuki, T. Uenoyama, and A. Yanase, "First-principles calculations of effective-mass parameters of AlN and GaN," *Phys. Rev. B* **52**(11), 8132–8139 (1995).
32. S. L. Chuang and C. S. Chang, "k·p method for strained wurtzite semiconductors," *Phys. Rev. B* **54**(4), 2491–2504 (1996).
33. S. L. Chuang and C. S. Chang, "A band-structure model of strained quantum-well wurtzite semiconductors," *Semicond. Sci. Technol.* **12**(3), 252–263 (1997).
34. S. H. Park, D. Ahn, and S. L. Chuang, "Electronic and optical properties of a- and m-plane wurzite InGaN-GaN quantum wells," *IEEE J. Quant. Electron.* **43**(12), 1175–1182 (2007).
35. D. Ahn and S. H. Park, "Theory of non-polar and semi-polar nitride semiconductor quantum-well structures," *Semicond. Sci. Technol.* **27**(2), 024011 (2012).
36. A. E. H. Love, *A Treatise on the Mathematical Theory of Elasticity*, Dover, New York (1944).
37. S. H. Park and S. L. Chuang, "Piezoelectric effects on electrical and optical properties of wurtzite GaN/AlGaN quantum well lasers," *Appl. Phys. Lett.* **72**(24), 3103–3105 (1998).
38. J. Piprek and S. Nakamura, "Physics of high-power InGaN/GaN Lasers," *IEEE Proc. Optoelectron.* **149**(4), 145–151 (2002).
39. S. Chichibu et al., "Effects of biaxial strain on exciton resonance energies of hexagonal GaN heteroepitaxial layers," *Appl. Phys. Lett.* **68**(26), 3766–3768 (1996).
40. M. Kumagai, S. L. Chuang, and H. Ando, "Analytical solutions of the block-diagonalized Hamiltonian for strained wurtzite semiconductors," *Phys. Rev. B* **57**(24), 15303–15314 (1998).
41. W. W. Chow et al., "Threshold conditions for an ultraviolet wavelength GaN quantum-well laser," *IEEE J. Selected Top. Quant. Electron.* **4**(3), 514–519 (1998).
42. W. Shan et al., "Pressure-dependent photoluminescence study of wurtzite GaN," *Appl. Phys. Lett.* **66**(25), 3492–3494 (1995).
43. K. Kim, W. R. L. Lambrecht, and B. Segall, "Elastic constants and related properties of tetrahedrally bonded BN, AlN, GaN, and InN," *Phys. Rev. B* **53**(24), 16310–16326 (1996).

44. S. H. Park and S. L. Chuang, "Comparison of zinc-blende and wurtzite GaN semiconductors with spontaneous polarization and piezoelectric field effects," *J. Appl. Phys.* **87**(1), 353–364 (2000).

45. P. D. C. King et al., "InN/GaN valence band offset: High-resolution x-ray photoemission spectroscopy measurements," *Phys. Rev. B* **78**(3), 033308 (2008).

46. S. H. Wei and A. Zunger, "Valence band splittings and band offsets of AlN, GaN, and InN," *Appl. Phys. Lett.* **69**(18), 2719–2721 (1996).

47. S. H. Park et al., "Intraband relaxation time effects on non-Markovian gain with many-body effects and comparison with experiment," *Semicond. Sci. Technol.* **15**(2), 203–208 (2000).

48. S. L. Chuang, *Physics of Optoelectronic Devices* John Wiley & Sons New York, pp 358–366 (1995).

49. S. H. Park and S. L. Chuang, "Crystal-orientation effects on the piezoelectric field and electronic properties of strained wurtzite semiconductors," *Phys. Rev. B* **59**(7), 4725–4737 (1999).

50. J. F. Muth et al., "Absorption coefficient, energy gap, exciton binding energy, and recombination lifetime of GaN obtained from transmission measurements," *Appl. Phys. Lett.* **71**(18), 2572–2574 (1997).

51. C. Reese et al., "Absolute internal quantum efficiency of an InGaN/GaN quantum well," in *IEEE Conference on Lasers and Electro-Optics (CLEO)*, IEEE, 472 (1996).

52. C. K. Sun et al., "Radiative recombination lifetime measurements of InGaN single quantum well," *Appl. Phys. Lett.* **69**(13), 1936–1938 (1996).

53. S. D. Donati, *Photodetectors, Devices, Circuits and Applications* , Prentice Hall, Upper Saddle River, NJ, pp. 369–379 (2000).

54. W. Zimmerman, "Experimental verification of the Shockley-Read-Hall recombination theory in silicon," *Electron. Lett.* **9**(16), 378–379 (1973).

55. D. McDonald et al. "Visualization of the intracellular behavior of HIV in living cells," *J. Cell Biol.* **159**(3), 441–452 (2002).

56. E. M. Campbell et al., "Labeling HIV-1 virions with two fluorescent proteins allows identification of virions that have productively entered the target cell," *Virology* **360**(2), 286–293 (2007).

57. W. Hubner et al., "Quantitative 3D video microscopy of HIV transfer across T cell virological synapses," *Science* **323**(5922), 1743–1747 (2009).

58. S. N. Gordon et al., "Short-lived infected cells support virus replication in Sooty Mangabeys naturally infected with simian immunodeficiency virus: implications for AIDS pathogenesis," *J. Virol.* **82**(7), 3725–3735 (2008).

59. A. G. Stern et al., "Intensity-imaging focal plane array using Geiger-mode avalanche photodiodes." Solid State Research Report MIT Lincoln Laboratory (**4**), 23–31 (2003).

60. A. G. Stern et al., "Digital photon-counting geiger-mode avalanche photodiode solid-state monolithic intensity imaging focal-plane with scalable readout circuitry," US Patent 7,858,917 (2010).

Alvin G. Stern has been involved with AG STERN, LLC, the company he founded in 2010. He earned his doctorate in electrical engineering at Boston University. He completed his bachelor of science degree in electrical engineering (BSEE) at Boston University in May of 2000. He was a member of the technical staff in the Advanced Imaging Technology Group at MIT Lincoln Laboratory for four years prior to returning to Boston University in 2004 to pursue PhD studies. He completed a master of science degree in electrical engineering (MSEE) in 2007, in the area of superconducting single photon detector (SSPD) characterization. Research interests include the design through analysis and simulation means, of solid-state silicon avalanche photodiode (APD) devices and their arrays for imaging applications. Research interests further include the design of high speed electronic readout circuits to control APD detector array operation.